iScience

CellPress
OPEN ACCESS

Article

Pharmacological targeting of Sam68 functions in colorectal cancer stem cells

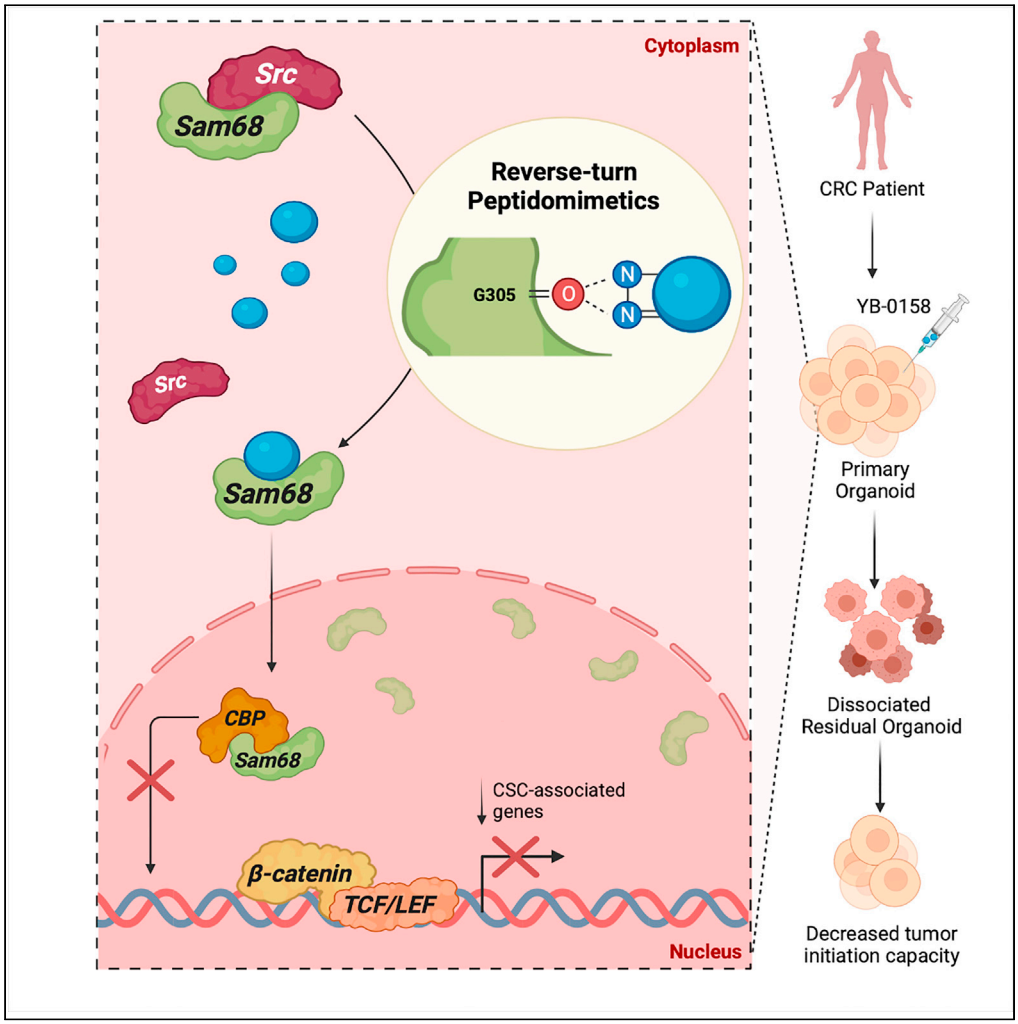

Angelique N. Masibag, Christopher J. Bergin, Joshua R. Haebe, ..., François M. Desrochers, Aube Fournier-Morin, Yannick D. Benoit

ybenoit@uottawa.ca

Highlights

Sam68 is a direct protein target of reverse-turn peptidomimetic small molecules

YB-0158 is a peptidomimetic structure with high predicted affinity for Sam68

YB-0158 elicits a cancer-selective response impeding main cancer stem cell hallmarks

YB-0158 blocks cancer stem cell activity in tumor organoids and *in vivo* systems

Masibag et al., iScience *24*, 103442
December 17, 2021
https://doi.org/10.1016/j.isci.2021.103442

iScience

CellPress
OPEN ACCESS

Article

Pharmacological targeting of Sam68 functions in colorectal cancer stem cells

Angelique N. Masibag,[1] Christopher J. Bergin,[1] Joshua R. Haebe,[1] Aïcha Zouggar,[1] Muhammad S. Shah,[1] Tamara Sandouka,[1] Amanda Mendes da Silva,[1] François M. Desrochers,[1] Aube Fournier-Morin,[1] and Yannick D. Benoit[1,2,*]

SUMMARY

Cancer stem cells (CSCs) are documented to play a key role in tumorigenesis and therapy resistance. Despite significant progress in clinical oncology, CSC reservoirs remain elusive and difficult to eliminate. Reverse-turn peptidomimetics were characterized as disruptors of CBP/beta-Catenin interactions and represent a promising avenue to curb hyperactive canonical Wnt/beta-Catenin signaling in CSCs. Recent studies suggested Sam68 as a critical mediator of reverse-turn peptidomimetics response in CSC populations. Using computational and biochemical approaches we confirmed Sam68 as a primary target of reverse-turn peptidomimetics. Furthermore, we executed an *in silico* drug discovery pipeline to identify yet uncharacterized reverse-turn peptidomimetic structures displaying superior anti-CSC activity in transformed pluripotent and colorectal cancer cell models. Thus, we identified YB-0158 as a reverse-turn peptidomimetic small molecule with enhanced translational potential, altering key hallmarks of human colorectal CSCs in patient-derived *ex vivo* organoids and *in vivo* serial tumor transplantation.

INTRODUCTION

Studies focused on tumor heterogeneity demonstrate continued support for the concept of cancer stem cells (CSCs), harboring self-renewal and tumor initiation capacities (Bergin et al., 2021; Kreso and Dick, 2014; Wainwright and Scaffidi, 2017). Notably, CSCs are suggested to play key roles in tumor recurrence, acquisition of chemo/radio-resistance, and the formation of metastases at distant sites (Boyd et al., 2018; Kreso et al., 2014). Despite significant progress in clinical oncology, CSC reservoirs remain elusive and difficult to eliminate (Dawood et al., 2014). Colorectal cancer (CRC) is among the deadliest neoplasms worldwide, and CRC tumors are organized according to a cellular hierarchy governed by CSC populations (Bergin et al., 2021; O'Brien et al., 2007). The canonical Wnt signaling pathway has been documented to be hyperactivated in CRC tumors and plays a central role maintaining CSC functions (Benoit et al., 2014). Thus, numerous strategies have been developed to target different aspects of such a molecular cascade, including its downstream transcriptional effector beta-Catenin (Benoit et al., 2014; Crespo et al., 2017; Jang et al., 2015).

Reverse-turn (or β-turn) peptidomimetic small molecules were reported as promising CSC-targeting agents, downregulating the transactivation of Wnt/beta-Catenin target genes (Emami et al., 2004). Specifically, β-turn peptidomimetics such as ICG-001 and CWP232228 were initially suggested as disruptors of the interactions between Wnt-dependent TCF/beta-Catenin transcriptional complexes and the histone acetyltransferase (HAT) CBP. As a result, β-turn peptidomimetics would curb transcriptional activation of canonical Wnt targets without altering the integrity of the upstream regulatory cascade. Although CBP/beta-Catenin interactions are mediated via several structural domains of CBP (e.g., TAZ and KIX domains) (Li et al., 2007), biochemical *in vitro* experiments suggested that β-turn peptidomimetic molecules bind to the adjacent nuclear receptor interacting domain (NRID) to block such interactions (Emami et al., 2004). However, recent studies shed light on alternative aspects of β-turn peptidomimetics mechanism of action by identifying Sam68 as a critical mediator of CWP232228 and ICG-001's antineoplastic response (Benoit et al., 2017). Thus, it is still unclear whether β-turn peptidomimetic molecules interact directly with CBP, beta-Catenin, and/or Sam68 in cancer cells (Wörthmüller and Rüegg, 2020). Although β-turn

[1]Department of Cellular and Molecular Medicine, University of Ottawa, Ottawa, ON K1H 8M5, Canada

[2]Lead contact

*Correspondence: ybenoit@uottawa.ca

https://doi.org/10.1016/j.isci.2021.103442

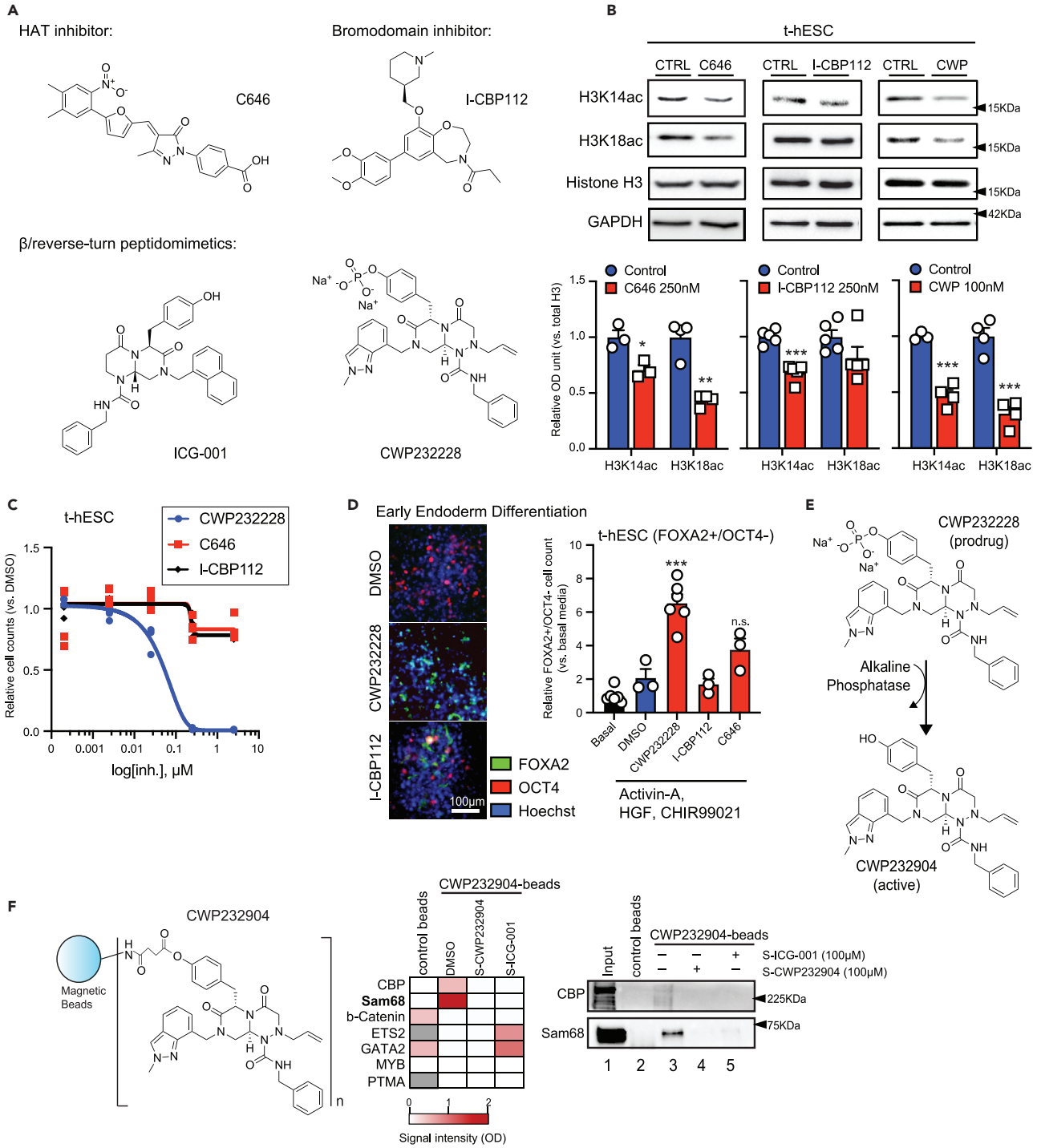

Figure 1. Reverse/β-turn peptidomimetic compounds are direct interactors of Sam68

(A) Chemical structure of HAT inhibitor C646 and bromodomain ligand I-CBP112, as well as β-turn peptidomimetics ICG-001 and CWP232228.

(B) Western blot analysis of CBP-catalyzed H3K14ac and H3K18ac histone acetylation marks in C646 (0.25 μM), I-CBP112 (0.25 μM), and CWP232228 (0.1 μM) t-hESCs versus control DMSO. Total histone H3 and GAPDH were used as loading control. Relative OD signal quantification versus H3 intensity is presented (C646: n = 3, I-CBP112: n = 5, CWP232228: n ≥ 3, *: p = 0.0183, **: p = 0.0078, ***: p ≤ 0.00033, two-tailed t test). Data are represented as mean ± SEM (error bars).

(C) Dose-response experiment assessing the impact of bromodomain ligand-based (C646 and I-CBP112), and peptidomimetic (CWP232228) inhibition of CBP on t-hESC growth (C646, I-CPB112: n = 4; CWP232228: n = 3).

Figure 1. *Continued*

(D) Early endoderm differentiation assay performed in t-hESCs in the presence of CWP232228 (0.1 μM, n = 6), I-CBP112 (0.25 μM, n = 3), or C646 (0.25 μM, n = 3) versus control DMSO (n = 6) and basal culture media (n = 3). Bar graph represents relative counts of FOXA2-positive (early endoderm marker)/OCT4-negative cells in DMSO, CWP232228, I-CBP112, and C646-treated t-hESCs versus basal culture media (one-way ANOVA, ***: $p < 0.0001$). Data are represented as mean ± SEM (error bars). Scale bar: 100 μm.

(E) Pro-drug CWP232228 is converted into its active form CWP231904 via hydrolysis of the phosphate group by serum/cellular alkaline phosphatase.

(F) Affinity pull-down experiments using CWP231904-conjugated magnetic beads performed on whole hESC lysates. Physical interaction between CBP, Sam68, beta-Catenin, ETS, MYB, GATA2, and PTMA with immobilized CWP231904 was assessed by immunoblotting. Each protein was previously shown as a member of the CBP interactome showing selective enrichment in human primary AML versus healthy blood (Benoit et al., 2017). Excess of soluble compounds (CWP and ICG001, 100 μM) were used to compete with immobilized CWP231904. Whole-cell lysate was used as input, and amine-functionalized beads were used as negative control (n = 2). The heatmap presents mean background-corrected OD signal for each putative interactor tested (gray: not tested).

peptidomimetics such as PRI-724 were recently tested in clinical trials, only mitigated success was obtained as an anticancer therapeutic agent. Despite showing elevated potential as CSC-targeting molecules at the biochemical level, it is crucial to extend our knowledge of the mechanism of action of β-turn peptidomimetics in human cancer to develop new analogous structures with enhanced translational value.

Here, we report the characterization of a small molecule (YB-0158) identified from an *in silico* Sam68 docking screening pipeline, altering key hallmarks of human colorectal tumorigenesis and presenting superior *in vivo* potency to block colorectal CSC activity.

RESULTS

Sam68 is a putative target of β-turn peptidomimetic molecules in cancer cells

Considering the co-activator function of CBP in the context of cancer, efforts were deployed to develop small molecules inhibiting its histone acetyltransferase activity. This led to the discovery and characterization of compounds selectively binding CBP/p300, such as the HAT inhibitor C646 and the bromodomain ligand I-CBP112 (Figure 1A) (Bowers et al., 2010; Conery et al., 2016). The small molecules ICG-001 and CWP232228 are two pioneer peptidomimetics that block CBP co-activator functions in cancer, causing a downregulation of beta-Catenin-dependent transcription (Figure 1A) (Emami et al., 2004; Jang et al., 2015). Cell growth and differentiation experiments in transformed human embryonic stem cells (t-hESCs), which provide a robust surrogate model of CSCs in culture, gave strikingly distinct results in side-by-side testing of CBP bromodomain inhibitors and β-turn peptidomimetics (Benoit et al., 2017). Although both C646 and I-CBP112 effectively reduced CBP-associated functions, either via downregulation of histone H3 acetylation marks (H3K14/18ac) or CBP levels (Figure 1B and S1A), only peptidomimetic-based inhibition achieved substantial growth reduction and endodermal differentiation onset in t-hESCs (Figures 1C and 1D). This further supports investigations on β-turn peptidomimetics as potential CSC-targeting therapies over other classes of small molecules directly interacting with CBP.

ICG-001 was initially reported as a disruptor of CBP/beta-Catenin interactions via the CBP NRID domain, thus inhibiting transactivation of canonical Wnt target genes (Eguchi et al., 2005; Emami et al., 2004). In human CSCs, the participation of the CBP binding partner Sam68 was recently identified as a critical mediator of β-turn peptidomimetics response (Benoit et al., 2017). Specifically, knocking down Sam68 or restricting its nuclear shuttling activity decreased cell growth in t-hESCs and human leukemia upon CWP232228 or ICG-001 treatments (Benoit et al., 2017). Thus, it is possible that ICG/CWP-like molecules are targeting factors other than NRID-dependent CBP/beta-Catenin interactions to block pro-oncogenic pathways. As we previously reported for other small molecules, we covalently immobilized the active form of CWP232228 (CWP231904) to solid beads and performed affinity purification assays using hESC lysates (Figures 1E and 1F) (Benoit et al., 2021). Binding of CWP231904 with CBP and six interactors previously shown as selectively upregulated in a neoplastic context (versus healthy counterpart) was profiled by immunoblotting (Figure 1F) (Benoit et al., 2017). We observed a clear interaction between CWP231904 and Sam68, while lower levels of CBP and other components of the Wnt pathway such as beta-Catenin were pulled down from pluripotent cell lysates (Figure 1F). Competition assays using excess of soluble CWP231904 or ICG-001 (100 μM each) validated the specificity of such interactions between immobilized ligand and Sam68 (Figure 1F). Notably, CWP232228 showed no impact on CBP and Sam68 levels in t-hESCs but reduced the amounts of active beta-Catenin supporting a reduction in canonical Wnt target gene expression (Figures S1A and S1B). Although β-turn peptidomimetics represent clear effectors of CBP, our observations strengthen the concept of Sam68 being a critical response mediator (Benoit et al., 2017), and potentially a direct target of such a class of small molecules in a pluripotent-like neoplastic context.

Direct binding of small molecules to Sam68 has been previously reported as a way to inhibit SH3-dependent interactions with Src (Oneyama et al., 2002). Specifically, the small molecule UCS15A was shown to disrupt Sam68 interactions with different SH3 motif-containing proteins in human HCT116 CRC cells, including Src, GRB2, and PLCγ (Oneyama et al., 2002). Extensive molecular investigations concluded that UCS15A blocks Sam68 protein-protein interactions by directly targeting its P4 and P5 proline-rich domains (Figure 2A) (Oneyama et al., 2002). We sought to determine whether it is possible to enhance β-turn peptidomimetics potency based on predicted Sam68 binding affinity. We built a structural model of a Sam68 fragment that includes P3 to P5 proline-rich domains (Sam68 275-374) using the TASSER-VMT algorithm and validated its quality using the composite scoring function QMEANDisCo (Studer et al., 2020). Plotting dihedral angles of the residues in our *in silico* model revealed 79.31% of highly preferred and 12.07% of preferred conformations (Figure S2A). Next, we compared the predicted 2D ligand-protein interaction diagrams for UCS15A and ICG-001 binding to Sam68 275-374 (Figure 2B). We observed a putative binding pocket shared by both compounds, implicating several common residues (Figure 2B). Using an *in silico* structural activity relationship approach (PyRx suite), we predicted the docking affinity for a collection of β-turn peptidomimetic analogs reported in the patent US8101751B2, as well as 16 random drug structures within the defined binding pocket (Figure 2C, Table S1) (Dallakyan and Olson, 2015). The analogs used in this analysis were selected based on the main structural variations between ICG-001 and active CWP232228 (CWP231904) (positions "A" and "B," Figure 2C).

In cell growth experiments, CWP232228 showed a strong cancer-selective growth inhibition toward human HT29 CRC cells (EC_{50}: 1.57 μM) versus normal intestinal progenitors HIEC cells (EC_{50}: >20 μM) (Figure 2D, Tables S1 and S2). ICG-001 also showed appreciable cancer-selective growth inhibition, but its EC_{50} value in CRC cells was substantially higher (EC_{50}: 14.6 μM) than that of CWP232228 (Figure 2D, Tables S1 and S2). In contrast, PRI-724 was more toxic to normal cells compared with the neoplastic model (Figure 2D). *In silico*, however, ICG-001 ranked among molecules with the highest predicted binding affinity for Sam68 275-374 (4/89), whereas other characterized β-turn peptidomimetics such as CWP231904 and hydrolyzed PRI-724 (PRI-724-OH), respectively, ranked 47/89 and 19/89 (Figure 2E, Tables S1 and S2) (Benoit et al., 2017; Tokunaga et al., 2017). Still, considering its ∼27-fold higher predicted docking affinity for the binding pocket within the Sam68 275-374 peptide versus UCS15A, its low EC_{50} and high cancer-selective toxicity in CRC cells versus other known β-turn peptidomimetics, the hydrolyzed form of CWP232228 (CWP231904) represents an optimal building block to design new candidates for *in vivo* applications.

To identify β-turn peptidomimetic structures with enhanced anticancer potency, we considered entities displaying optimal predicted Sam68 binding and highest similarity to CWP232228 with the prospect to maintain bioactive properties. By applying a chemical structure similarity analysis to our main Sam68 275-374 binding candidates, we identified a putative β-turn peptidomimetic structure (YB-0159) with a Tanimoto coefficient of 0.9601 (1/88) and a predicted docking affinity ∼3-fold higher (18/89) versus CWP231904 (Figure 2F and S2B, Tables S1 and S2). The putative prodrug structure was named YB-0158 and includes a hydrolyzable phosphate moiety similar to CWP232228. YB-0158 presents an 1H-indazole function in position "B" instead of the 2-methyl-2H-indazole found in CWP232228 (Figure 2F, Tables S1 and S2). Such a function was predicted to form two hydrogen bonds (3.04 and 2.80 Å) between nitrogen N7 and N6 of YB-0159 and glycine 305 within the defined binding pocket of Sam68 (Figures 2G andS2C). Upon *in silico* substitution of G305 in Sam68 275-374 (G305A, G305N, G305S), we repeated docking analysis for both YB-0159 and CWP231904 and observed significantly reduced binding affinity between YB-0159 and Sam68 274-374 (Figure S2D and S2E, Table S2). Remarkably, none of the G305 substitutions had a significant impact on the predicted docking energy of CWP231904, further supporting the implication of the 1H-indazole function in Sam68 binding (Figure S2E, Table S2).

The reverse-turn peptidomimetic YB-0158 exhibits enhanced potency in colorectal CSCs

To determine the relevance of the YB-0158 structure as an antineoplastic agent, we proceeded to small molecule synthesis and characterized its bioactivity (Figure S2F, Data S1). Dose-response experiments confirmed that YB-0158 displays ∼10- and ∼5-fold higher potency versus CWP232228 for growth inhibition in t-hESCs and HT29 CRC cells, respectively (Figures 3A and 3B). As previously demonstrated for CWP232228, YB-0158 also induced a loss of pluripotency in t-hESC, characterized by a decrease in OCT4-positive cells (Figure S3A) (Benoit et al., 2017). This supports the potential of YB-0158 to alter pluripotent-like transcriptional signatures in a neoplastic context (Ben-Porath et al., 2008; Bergin et al., 2021; Sachlos et al., 2012). Akin to CWP232228, YB-0158 treatments disrupted Sam68-Src interactions in CRC cells,

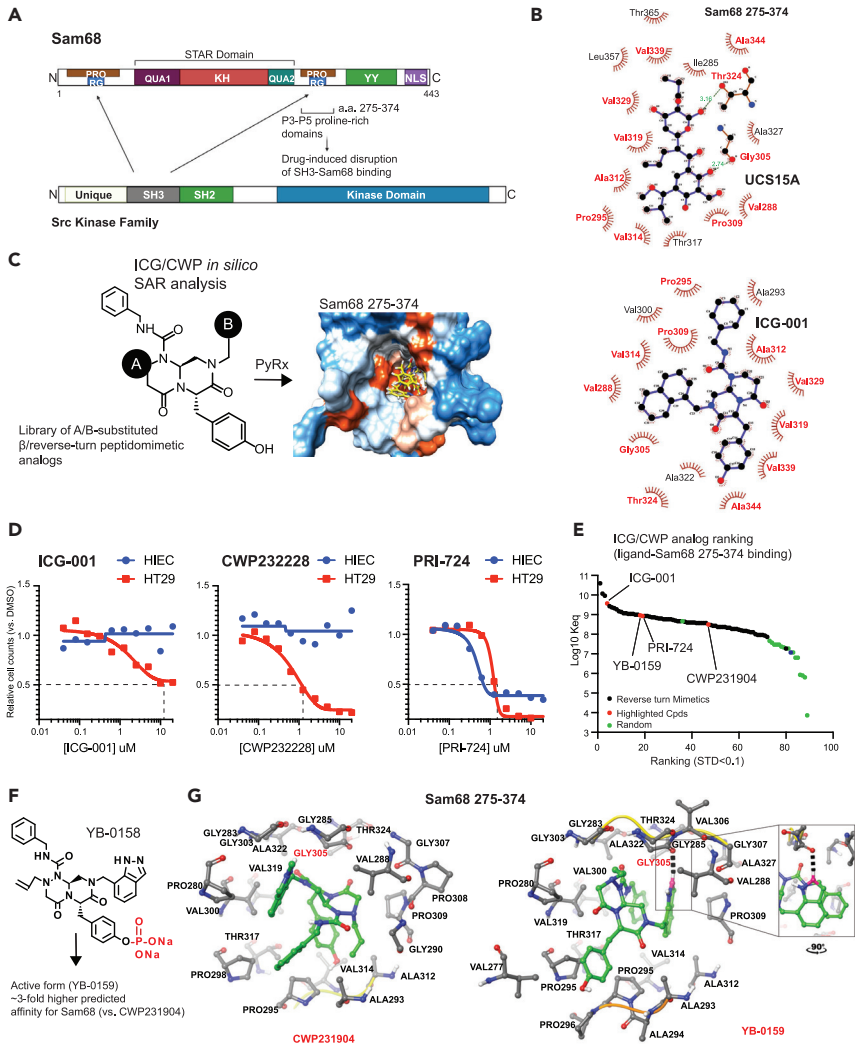

Figure 2. *In silico* screening of peptidomimetics with enhanced binding affinity for Sam68

(A) Representation of Sam68 interacting with SH3 domain in Src kinase family proteins via proline-rich motifs located in N-terminal P1-P2 and between residues 275 and 374 (P3, P4, P5). Small molecule UCS15A is known to disrupt SH3-mediated interaction of Src with Sam68 P3-5 domains (Sharma et al., 2001).

(B) 2D representation of UCS15A and the peptidomimetic ICG-001 *in silico* predicted binding pocket in Sam68 275-374 peptide (red, oxygen; blue, nitrogen). Common residues involved in both small-molecule-binding pockets are highlighted in red. Predicted hydrogen bond length is represented by dashed lines (Å).

(C) Schematic representation of the *in silico* structure-activity relationship analysis pipeline (PyRx) used to identify β-turn peptidomimetic molecules with enhanced binding affinity for Sam68 275-374 domain. "A" and "B" represent the positions of distinct substituents added to reverse-turn mimetic cores.

(D) Dose-response curves assessing selective toxicity of peptidomimetics ICG-001, CWP232228, and PRI-724 in HT29 human colorectal cancer cell line versus normal intestinal progenitor cells HIEC ($n \geq 4$, 48-h treatments).

(E) Compound ranking based on predicted Keq for each β-turn analog (black dots). Only molecules presenting a standard deviation below 0.1 for a minimum of three analysis runs, with an exhaustiveness ("E") level of "8" were plotted. Dots corresponding to ICG-001, CWP231904, PRI-724-OH, and YB-0159 were highlighted in red. Random structure ranking is represented by green dots. See also Table S1.

(F) Structure of YB-0158, a phosphate-stabilized prodrug of YB-0159.

(G) Docked poses of CWP231904 (left) and YB-0159 (right) in human Sam68 257-374 fragment (red, oxygen; blue, nitrogen). Glycine 305 is highlighted in red, where distinct hydrogen bond (gray dashed line) was predicted between YB-0159 and Sam68. The inset in the right pose represents a higher magnification view of the predicted hydrogen bond formation between YB-0158 and Gly305.

See also Table S2.

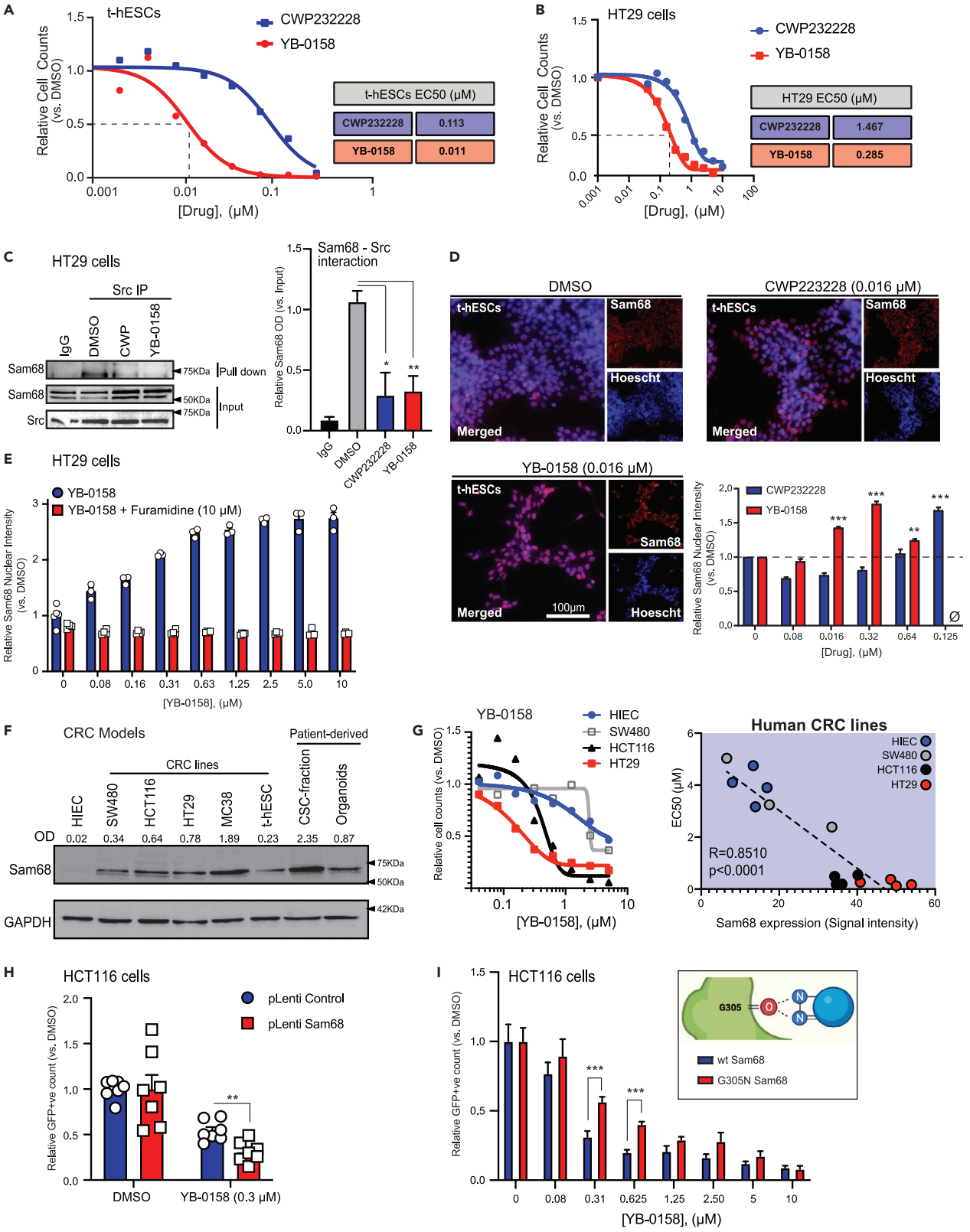
A
t-hESCs
CWP232228
YB-0158
Relative Cell Counts (vs. DMSO)
[Drug], (μM)
t-hESCs EC50 (μM)
CWP232228 0.113
YB-0158 0.011
B
HT29 cells
CWP232228
YB-0158
Relative Cell Counts (vs. DMSO)
[Drug], (μM)
HT29 EC50 (μM)
CWP232228 1.467
YB-0158 0.285
C
HT29 cells
Src IP
IgG
DMSO
CWP
YB-0158
Sam68
Src
75KDa
50KDa
Pull down
Input
Sam68 - Src interaction
Relative Sam68 OD (vs. Input)
D
DMSO
CWP223228 (0.016 μM)
YB-0158 (0.016 μM)
t-hESCs
Sam68
Hoescht
Merged
100μm
Relative Sam68 Nuclear Intensity (vs. DMSO)
[Drug], (μM)
E
HT29 cells
YB-0158
YB-0158 + Furamidine (10 μM)
Relative Sam68 Nuclear Intensity (vs. DMSO)
[YB-0158], (μM)
F
CRC Models
Patient-derived
CRC lines
HIEC
SW480
HCT116
HT29
MC38
t-hESC
CSC-fraction
Organoids
OD 0.02 0.34 0.64 0.78 1.89 0.23 2.35 0.87
Sam68
GAPDH
75KDa
50KDa
42KDa
G
YB-0158
HIEC
SW480
HCT116
HT29
Relative cell counts (vs. DMSO)
[YB-0158], (μM)
Human CRC lines
EC50 (μM)
R=0.8510
p<0.0001
Sam68 expression (Signal intensity)
H
HCT116 cells
pLenti Control
pLenti Sam68
Relative GFP+ve count (vs. DMSO)
DMSO
YB-0158 (0.3 μM)
I
HCT116 cells
G305
wt Sam68
G305N Sam68
Relative GFP+ve count (vs. DMSO)
[YB-0158], (μM)

Figure 3. YB-0158 alters Sam68 biology in human cancer cells

(A) Dose-response experiment assessing growth inhibition caused by peptidomimetics analogs CWP232228 and YB-0158 in t-hESCs (n = 3, 48-h treatments). Calculated EC_{50} for each small molecule is presented in the inset table. See also Data S1.

(B) Dose-response experiment assessing growth inhibition caused by peptidomimetic analogs CWP232228 and YB-0158 in HT29 colorectal cancer cells (n = 2, 48-h treatments). Calculated EC_{50} for each small molecule is presented in the inset table.

(C) Co-immunoprecipitation (IP) assessing changes in interaction levels between Src and Sam68 in response to CWP232228 (1.5 μM) and YB-0158 (0.3 μM) in HT29 cells (48 h) (n = 3, *: p = 0.021, **: p = 0.0088, two-tailed t test). Data are represented as mean ± SEM (error bars). Mouse IgGs were used as negative control for pull down.

(D) Immunofluorescence staining of Sam68 in DMSO, CWP232228, and YB-0158-treated t-hESCs (48 h, n = 9). Quantification of nuclear Sam68 was performed by high-content imaging and presented as relative levels versus DMSO (**: p < 0.01, ***: p < 0.0001, two-tailed t test). Data are represented as mean ± SEM (error bars). Scale bar: 100 μm.

(E) Quantification of nuclear Sam68 in HT29 cells treated with increasing doses of YB-0158, in the presence (n = 4) or absence (n = 3) of a PRMT1 inhibitor (Furamidine, 10 μM). Cells were treated for 48 h and nuclear Sam68 immunostaining was quantified by high-content imaging. Data are represented as mean ± SEM (error bars).

(F) Western blot analysis of Sam68 levels in normal human intestinal progenitor cells HIEC; human colorectal cancer SW480, HT29, and HCT116 lines; mouse colon adenocarcinoma MC38 cells; t-hESCs; as well as patient-derived CSC-enriched spheroids and 3D organoids from colorectal tumor samples (n ≥ 3). Relative OD signal quantification for Sam68 versus loading control (GAPDH) is presented.

(G) Dose-response experiment monitoring growth of normal intestinal cells HIEC, as well as HT29, SW480, and HCT116 colorectal cancer lines treated with YB-0158 (n ≥ 3, 48 h). A significant correlation was established between calculated EC_{50} and Sam68 expression (R^2 = 0.8510, p < 0.0001, simple linear regression).

(H) Cell growth experiment in HCT116 cells transduced with control/empty-mGFP (pLenti Control) or *KHDRBS1*-mGFP (pLenti Sam68) overexpression vectors and treated with YB-0158 (0.3 μM, 48 h) or vehicle control (DMSO). GFP-positive cell counts upon treatments are presented versus their corresponding DMSO-treated group (n = 7, **: p = 0.003, two-tailed t test). Data are represented as mean ± SEM (error bars).

(I) Cell growth experiment using HCT116 cells overexpressing wild-type Sam68 (*KHDRBS1*) (wt Sam68) or with a mutated G305 motif (G305N Sam68) and subjected to increasing doses of YB-0158 (0.08–10 μM versus DMSO control) for 48 h. Residual transduced cells (GFP reporter) were counted for each dose and presented versus DMSO control (n ≤ 5, ***: p < 0.001, two-tailed t test). Data are represented as mean ± SEM (error bars).

when used at calculated EC_{50} concentrations (Figure 3C). Moreover, no changes in Src Y416 phosphorylation status were noted upon YB-0158 or CWP232228 treatments, supporting previous findings indicating that small molecule-based disruption of Sam68-SH3 interactions has no impact on Src autophosphorylation kinase activity (Figure S3B) (Sharma et al., 2001). Loss of Sam68-Src interactions upon YB-0158 treatments was accompanied with significant accumulation of Sam68 in the nucleus of both t-hESCs and HT29 cells (Figures 3D and S3C). This is consistent with previous observations made for CWP232228 and ICG-001 in t-hESCs (Benoit et al., 2017). Lower doses of YB-0158 were also sufficient to induce significant Sam68 accumulation (<0.064 μM) compared with CWP232228 (≥0.125 μM) in t-hESCs (Figure 3D). Previous studies revealed that asymmetric demethylation of Sam68 R304 residue (within P3-P5 proline-rich domain) by PRMT1 is essential to its nuclear translocation (Côté et al., 2003). Thus, we used furamidine to inhibit PRMT1 activity in HT29 cells and observed that YB-0158 was no longer able to stimulate Sam68 nuclear accumulation upon PRMT1 inhibition (Figures 3E and S3D). Sam68 nuclear shuttling following β-turn peptidomimetic treatments was also associated with enhanced formation of Sam68-CBP complexes and sequestration of CBP from the chromatin (Benoit et al., 2017; Hong et al., 2002b). Hence, YB-0158 and CWP232228 used at EC_{50} similarly decreased CBP recruitment at the promoter of Wnt/beta-Catenin target genes *LGR5* and *MYC* in HT29 cells, compared with DMSO control (Figure S3E).

To assess the potential of Sam68 as a preferential target for β-turn peptidomimetics in CRC, we profiled transcript expression of key factors involved in the molecular mechanism of action of such small molecules in primary colon (COAD) and rectal (READ) adenocarcinomas (Figure S3F). Sam68 (*KHDRBS1*) mRNA expression was significantly overexpressed in colon and rectal tumors compared with healthy tissues, whereas no differences were observed for CBP (*CREBBP*) mRNA levels (Figure S3F). Similar observations were made in various human and murine CRC models, where Sam68 protein levels were elevated in cancerous lines (SW480, HCT116, HT29, MC38), whereas only trace expression was detected in normal human intestinal progenitor cells HIEC (Figure 3F). Sam68 expression was also higher in CSC-enriched spheroids derived from patients with CRC versus heterogeneous bulk tumor organoids (Figure 3F) (Bergin et al., 2021). Importantly, we established a direct relationship between Sam68 protein levels and YB-0158 response (EC_{50}) in human intestinal models (Figure 3G).

Next, we modulated Sam68 expression in CRC cells and evaluated the impact on YB-0158 responses. Knockdown of Sam68 followed by growth assessments in drug-treated HT29 cells revealed significant decreases in YB-0158 potency, where an ∼2-fold increase of EC_{50} was observed compared with scrambled shRNA control cells (EC_{50} sh*KHDRBS1*: 0.625 μM, EC_{50} shCTRL: 0.290 μM) (Figure S3G). Such a

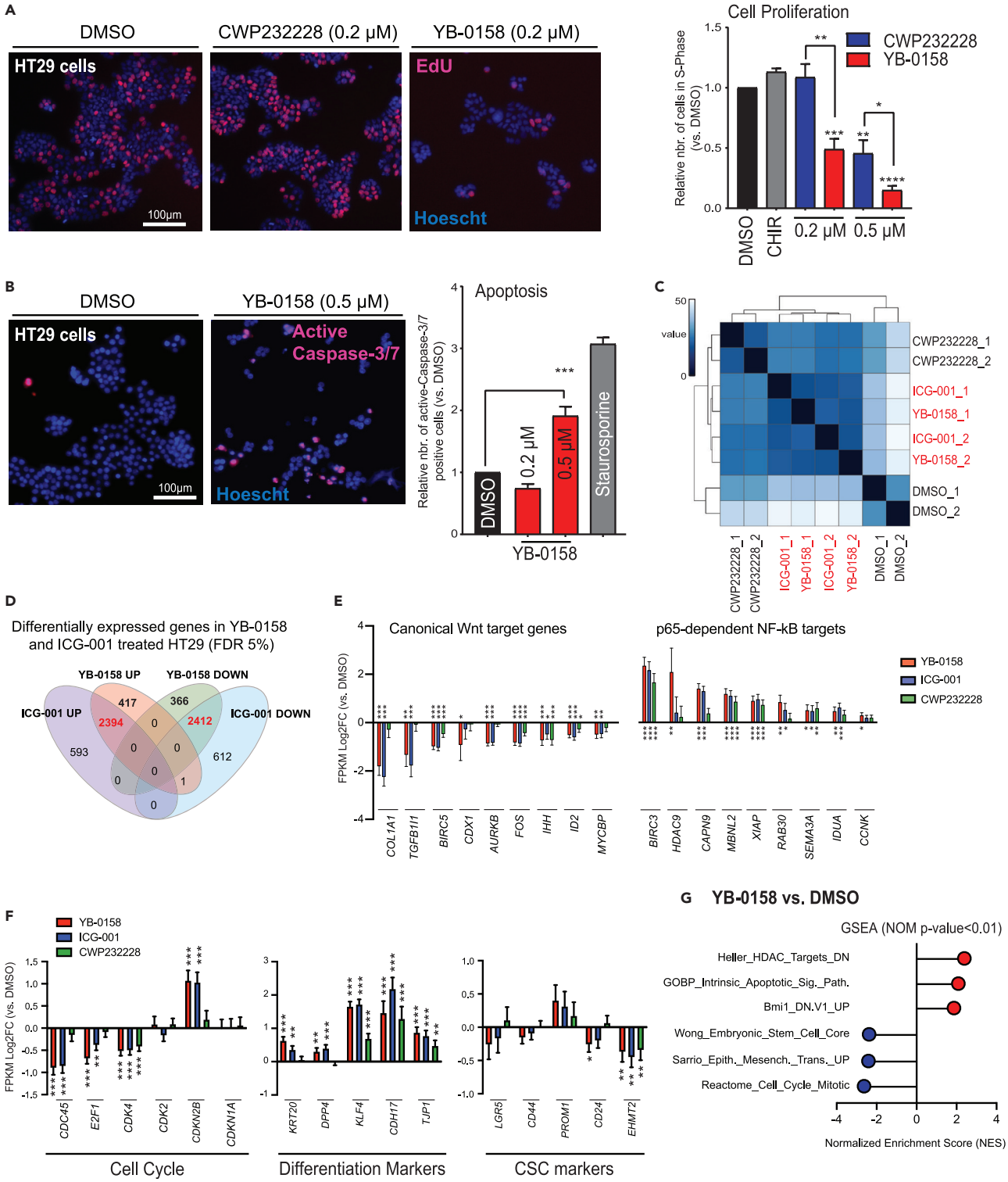

Figure 4. YB-0158 impacts proliferation, apoptosis, and differentiation in human colorectal cancer cells

(A) EdU incorporation assay labeling cells in S-phase indicates proliferation rates in CWP232228 and YB-0158-treated (48 h) HT29 cells versus DMSO control. CHIR99021 was used as a canonical Wnt activation control (3 μM). The relative number of EdU-positive cells was determined by high-content imaging ($n \geq 3$, *: $p = 0.0257$, **: $p \leq 0.0017$, ***: $p < 0.0001$, two-tailed t test). Data are represented as mean ± SEM (error bars). Scale bar: 100 μm.

(B) *In situ* fluorescent staining of activated Caspase-3/7 in YB-0158-treated HT29 cells (48 h, 0.2 μM and 0.5 μM) compared with DMSO control. Staurosporine (6 h, 1 μM) was used as a positive control for apoptosis induction ($n = 3$, ***: $p < 0.0001$, two-tailed t test). Data are represented as mean ± SEM (error bars). Scale bar: 100 μm.

Figure 4. *Continued*

(C) Clustering analysis of transcriptional responses to ICG-001 (10 μM), CWP232228 (1.5 μM), and YB-0158 (0.3 μM) versus DMSO control in HT29 cells (48 h, RNA-seq, n = 2). Transcriptomes of ICG-001 and YB-0158-treated cells showed the highest level of similarity (highlighted in red).

(D) Venn diagram of significantly modulated genes (versus DMSO control) in HT29 cells treated with 0.3 μM YB-0158 or 10 μM ICG-001 (48 h, n = 2, $p < 0.05$, FDR $q < 0.05$). Numbers of commonly modulated genes by both compounds are highlighted in red. See also Table S3.

(E) Transcript expression of canonical Wnt and p65-dependent NF-kB target genes in response to ICG-001 (10 μM), CWP232228 (1.5 μM), and YB-0158 (0.3 μM) in HT29 cells (48 h, RNA-seq, n = 2, *: $p \leq 0.0457$, **: $p \leq 0.0100$, ***: $p \leq 0.0009$, DESeq2 Benjamini-Hochberg corrected). Values are expressed as log2 fold-changes (L2FC) +/− SEM (error bars) versus DMSO controls. See also Table S3.

(F) Transcript expression of cell cycle regulators, intestinal differentiation markers, and colorectal CSC markers in response to ICG-001 (10 μM), CWP232228 (1.5 μM), and YB-0158 (0.3 μM) in HT29 cells (48 h, RNA-seq, n = 2, *: $p = 0.019$, **: $p \leq 0.010$, ***: $p \leq 0.0003$, DESeq2 Benjamini-Hochberg corrected). Values are expressed as (L2FC) +/− SEM (error bars) versus DMSO controls. See also Table S3.

(G) Gene enrichment signature analysis (GSEA) of YB-0158 transcriptional response ($p < 0.05$, FDR $q < 0.05$) versus DMSO control in HT29 cells showing correlations with intrinsic apoptosis, HDAC targets downregulation, and Bmi1 target gene signatures. Significant negative enrichment was observed for pro-mitotic, upregulated EMT, and ES cell core gene signatures. No significant correlation was established with Wnt target gene signatures. Normalized enrichment scores are presented and only nominal p values <0.05 were considered significant.

See also Table S4.

phenomenon was not observed in CBP knockdown HT29 cells versus control shRNA (Figure S3H). Moreover, we used a lentiviral transduction system to overexpress Sam68 in HCT116 cells versus an empty/control vector (Figure S3I). Cell count experiments revealed that Sam68 overexpression significantly increased the potency of YB-0158 for growth inhibition compared with control cells (Figure 3H). Finally, we overexpressed a mutant of Sam68 predicted to decrease its affinity for YB-0158 (G305N) in HCT116 cells (Figure S2E) and tested the impact of altering such a motif on YB-0158 response. We observed a significant decrease of YB-0158 potency in G305N mutant overexpressing cells compared with wild-type Sam68 overexpression, at doses ranging from 0.31 to 0.625 μM (Figures 3I and S3I). Altogether, these observations support a direct targeting of Sam68 by β-turn peptidomimetics such as YB-0158 and highlights the relevance of Sam68 G305 motif in mediating such an interaction.

EdU incorporation confirmed that lower doses of YB-0158 were sufficient to significantly decrease proliferation in human CRC cells compared with CWP232228 (Figure 4A). When used at 0.5 μM, YB-0158 also significantly increased apoptosis in CRC cells as represented by activated Caspase-3/7 detection assays (Figure 4B). To expand our understanding of YB-0158's functional impact in CRC, we profiled global transcriptional changes induced by this peptidomimetic small molecule, along with closely related ICG-001 and CWP232228 in CRC cells. All three compounds were used at their respective EC_{50} in HT29 cells to get similar responses at the functional level. Whole transcriptome clustering analysis revealed that YB-0158's transcriptional response in CRC cells is highly similar to ICG-001, compared with CWP232228 (Figures 4C, 4D,S4A, and S4B). This is unexpected considering the higher structural similarity between YB-0158 and CWP232228, compared with ICG-001 (Figure 2). However, both YB-0158 and ICG-001 displayed superior theoretical Sam68-binding capacities versus CWP232228, which may represent a plausible explanation (Figure 2D, Tables S1 and S2).

The downregulation of key genes extensively associated with the effect of β-turn peptidomimetics on canonical Wnt targets, such as *BIRC5*, and the colorectal CSC marker *LGR5* was validated by quantitative PCR in CRC cells treated with YB-0158 (versus DMSO control) (Figure S4C) (Arensman et al., 2014; Benoit et al., 2017). In addition, the analysis of differentially modulated genes upon YB-0158 treatments (versus DMSO) showed a significant downregulation of several other canonical Wnt target genes (Figure 4E). Considering that the influence of Sam68 on transcriptional regulation is not limited to Wnt/beta-Catenin, we evaluated the impact of YB-0158 on the expression of downstream targets nuclear factor κB (NF-kB), previously shown to be downregulated by Sam68 nuclear translocation in cancer and promoting key antineoplastic effects (Fu et al., 2016). We observed an upregulation of several documented p65-dependent NF-kB target genes in response to YB-0158 (Figure 4E, Table S3). The modulation of canonical Wnt and NF-kB target genes caused by YB-0158 was generally recapitulated by the other β-turn peptidomimetics that we tested (ICG-001 and CWP232228) (Figure 4E, Table S3).

In accordance with the role of Wnt/beta-Catenin stimulating cell proliferation and self-renewal, YB-0158 treatments decreased the expression of positive cell cycle regulators *CDC45*, *E2F1*, and *CDK4*, combined with increased expression of the proliferation inhibitor *CDKN2B* (Figure 4F, Table S3). Moreover, several intestinal differentiation and cell polarization markers such as *KRT20*, *DPP4*, *KLF4*, *CDH17* (Li-Cadherin), and *TJP1* (ZO1) were upregulated by YB-0158 treatments, indicative of reduced malignancy in surviving

cells (Figure 4F, Table S3) (Benoit et al., 2012; Bergin et al., 2021; Lepage et al., 2018). Accordingly, RNA sequencing experiments showed significant downregulation of colorectal CSC markers *CD24* and G9a (*EHMT2*) in HT29 cells upon YB-0158 treatments (Figure 4F, Table S3) (Bergin et al., 2021; Hatano et al., 2017). In most cases, the impact of YB-0158 on genes highlighted in Figure 4F was mimicked by ICG-001 treatments but not by CWP232228 (Figure 4F).

Gene signature enrichment analyses (GSEAs) also supported the anti-proliferative and pro-apoptotic effects of YB-0158 in human CRC cells. Specifically, the transcriptional signature associated with YB-0158 treatments was positively correlated with gene expression related to intrinsic apoptotic signaling and p53 pathways, whereas it negatively correlated with cell cycle progression through mitosis and MYC target expression (Figures 4G and S4D, Table S4). Moreover, GSEAs revealed that the YB-0158 transcriptional response correlated with different gene expression signatures to support a loss of pluripotency (Wong_Embryonic_Stem_Cell Core), decreased self-renewal activity (Bmi1_DN.V1_UP), and reduced epithelium to mesenchyme transition (EMT) (Sarrio_EMT_UP) via enhanced organization of epithelial cell junctions (Onder_CDH1_targets_UP, GOBP_Positive_Reg_Cell_Junction_Assembly) (Figure 4G and S4D, Table S4). Such characteristics associated to CSC biology are supported by a negative correlation between the YB-0158-specific transcriptome and genes upregulated by sonic hedgehog, previously reported as a hallmark of colorectal CSCs (Figure S4D, Table S4) (Lima-Fernandes et al., 2019). Taken together, our functional genomic analysis presents YB-0158 as an important modulator of colorectal CSC properties but not exclusively through the inhibition of canonical Wnt targets. YB-0158-dependent modulation of Sam68 could also affect other important pathways in colorectal cancer, including NF-kB.

To further explore the functional role of YB-0158 in human colorectal CSCs we used a serial organoid formation assay and tested the potential of YB-0158 to affect the tumor-initiating capacity of primary CRC samples (Figure 5A). Patient-derived organoids (PDOs) enable the study of human solid tumors initiated from a single stem cell in a 3D system, recapitulating functional and morphological characteristics of primary tissues, and predicting drug response in a pre-clinical *in vivo* setting (Bergin et al., 2021; Tuveson and Clevers, 2019). Colorectal CSC enrichment from spheroid cultures was previously demonstrated by our group via profiling of markers such as CD133, CD44, LGR5, and G9a versus bulk tumor sample (Bergin et al., 2021). The clinical information about the patient-derived specimens used in this study is presented in Figure 5B. A series of primary organoids was exposed to doses of YB-0158 ranging from 0.125 to 2 μM (versus DMSO control) and resulted in a significant decrease in total organoid counts compared with vehicle-treated groups (Figures 5C and S5A). Residual primary organoids were dissociated and re-seeded in a secondary series with no further drug treatments, enabling bona fide assessment of persisting tumor-initiating cell populations (Figure 5A). Thus, we observed that YB-0158-treated primary organoids had a significantly lower tumor-initiating capacity when plated in a secondary assay, confirming the potential of our peptidomimetic small molecule of interest to restrict human colorectal CSC functions (Figures 5C and S5B) (Bergin et al., 2021).

Subsequently, we tested the potential of YB-0158 to eliminate colorectal CSC activity *in vivo*, within a murine syngeneic serial tumor transplantation model (Figure 5D) (Jinushi et al., 2011). Akin to serial PDO assays, the detection of a tumor graft in untreated secondary mouse recipients indicates the presence of active CSC populations (Benoit et al., 2017). Thus, we injected 5 x 10^5 MC38 (murine colon adenocarcinoma) cells in the flanks of C57BL/6 mice and performed daily IP injections of YB-0158, CWP232228, and control saline from day 7 post engraftment, over a period of 14 days (Figure 5D). We used both compounds at doses of 100 mg/kg, based on previous *in vivo* experiment studying the impact of CWP232228 on CSC activity (Benoit et al., 2017; Kim et al., 2016). Although YB-0158 displayed a lower EC_{50} (1.64 μM) compared with CWP232228 (3.47 μM) in cultured MC38 cells, no significant differences in primary tumor size were observed upon either YB-0158 or CWP232228 *in vivo* treatments versus saline controls (Figures 5E, S5C, and S5D). Following drug treatments (day 21), the tumors from primary recipient mice were harvested and dissociated for re-transplantation into secondary recipients (Figure 5D). We observed a significant decrease in secondary tumor formation frequency in the YB-0158 group compared with saline controls, indicating that drug treatments in primary recipients suppressed CSC activity in 69% (11/16) of secondary animals (Figure 5F). In contrast, only 45% (9/20) of secondary mice engrafted with tumor cells from CWP232228-treated primary recipients showed no CSC activity, and the difference in tumor formation frequency was not statistically significant versus saline controls (Figures 5F and S5E). Moreover, residual secondary tumors from YB-0158-treated group were significantly smaller versus matched saline controls, whereas such a phenomenon was not seen in secondary recipients from the CWP232228 group (Figure S5F).

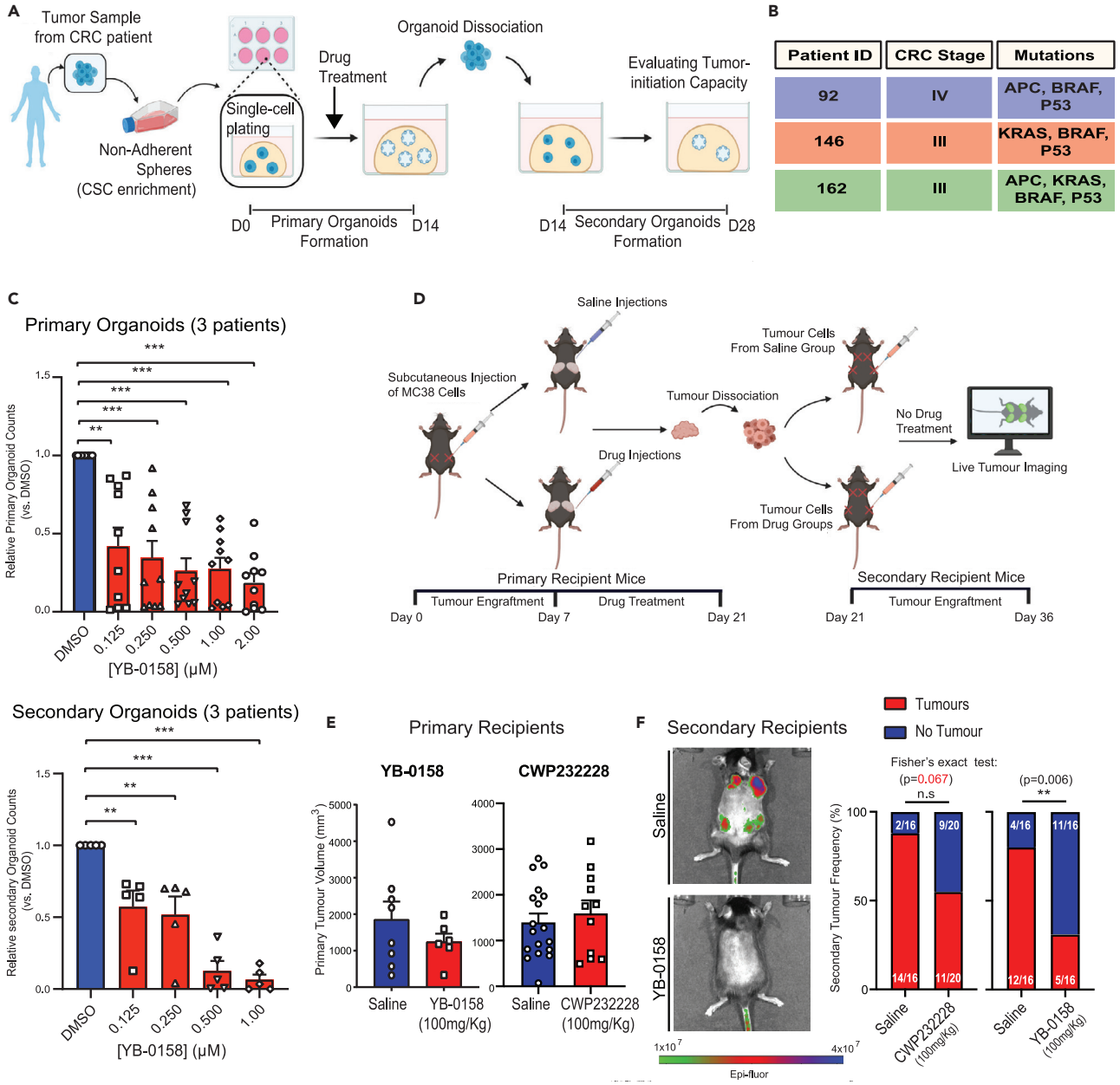

Figure 5. Impact of YB-0158 on CSC activity in colorectal cancer, using patient-derived and *in vivo* systems

(A) Schematic representation of serial organoid formation assay using primary human colorectal tumor tissues. CSC fraction is enriched in non-adherent spheroid cultures (Bergin et al., 2021).

(B) Clinical information available for patients with colorectal cancer involved in serial organoid experiments. Patient ID #92: 45-year-old, female. Patient ID #146: 65-year-old, male. Patient ID #162: 63-year-old, female. No gender information is available.

(C) Primary organoid formation frequency observed upon YB-0158 treatments (upper panel, increasing doses from 0.125 to 2 µM versus DMSO, 7 days), and organoid formation frequencies observed in secondary plating assays (lower panel, DMSO and YB-0158: 0.125 to 1 µM). Organoid counts were normalized versus DMSO controls (three patients, n = 10, **: $p < 0.01$, ***: $p < 0.0001$, two-tailed t test). Data are represented as mean ± SEM (error bars).

(D) Schematic representation of the murine syngeneic serial tumor transplantation assay used to measure CSC activity *in vivo*. Only primary mouse recipients are treated with YB-0158 or CWP232228 (100 mg/kg). Presence/absence of secondary tumors is determined by live fluorescence tumor imaging (IVIS, IRDye 800CW 2-DG, 10 nM per mouse).

(E) Tumor volume (mm^3) from primary mouse recipients treated with daily 100 mg/kg IP injections of YB-0158 (n = 8) or CWP232228 (n = 11) over 14 days versus control saline and measured at day 21 post engraftment. Data are represented as mean ± SEM (error bars).

(F) Frequency of secondary tumors observed in YB-0158 (n = 16) and CWP232228 (n = 20), versus respective control saline groups on day 36. Representative live fluorescence tumor images are shown for saline and YB-0158 animals (Fisher's exact test: drug versus saline, **: p = 0.006, n.s: p = 0.067). Data are represented as percentage of tumor frequency.

Macroscopic observations of mouse behavioral and clinical indicators, including weight loss, feces consistency, rectal bleeding, movement disorder, facial grimace, abnormal respiration, hunching, piloerection, agitation/aggressivity, food consumption, and grooming habits revealed no significant differences between control and drug-treated (CWP232228 and YB-0158) animals. Moreover, we determined that YB-0158 treatments did not cause alterations of normal intestinal mucosae architecture (distal ileum) compared with saline-injected mice (Figure S5G). We observed no significant changes in the number of proliferative cells per crypt (Ki-67^{+}) and average villus length in the normal intestinal tissues of YB-0158 or CWP232228-treated mice compared with controls (Figure S5H). Considering that YB-0158 shows no significant effects on normal intestinal tissue homeostasis, these histological data support the cancer-selective toxicity exhibited by our peptidomimetic compound of interest in human cell models. Still, additional studies will be necessary to extensively assess its clinical safety. Altogether, our pre-clinical investigations highlight the potential of YB-0158 as a potent colorectal CSC targeting agent.

DISCUSSION

The reverse/β-turn class of peptidomimetics were extensively documented as promising pharmacological strategies to target several types of neoplastic cells, including CSCs (Benoit et al., 2017; Chan et al., 2015; Jang et al., 2015; Kim et al., 2016). Despite the cancer-selective aspect of such a class of molecules, mainly attributed to CBP/beta-Catenin disruption, we noted mitigated developments on β-turn peptidomimetics in clinical testing and progress toward late trial phases. To our knowledge, no clinical trials involved ICG-001 or CWP232228 as potential cancer therapies, and PRI-724 demonstrated only modest clinical activity in advanced pancreatic adenocarcinomas (Ko et al., 2016). Thus, with the characterization of YB-0158, our study highlights the possibility to improve the efficacy of such compounds to enhance their therapeutic index and facilitate their development as powerful antitumor and CSC-targeting agents.

Our affinity pull-down assays confirmed the capacity of CWP232228 to bind to Sam68 in human cells, and an excess of soluble ICG-001 effectively outcompeted such an interaction (Figure 1F). To date, UCS15A was the only small molecule inhibitor to be experimentally supported as a direct Sam68 interactor. Interestingly, another CWP peptidomimetic compound with an undisclosed structure (CWP-291) was also suggested to interact with Sam68 in cancer cells (Cortes et al., 2015; Wörthmüller and Rüegg, 2020). CWP-291 was clinically investigated in phase 1 studies and was deemed safe and effective as a monotherapy to target hematological malignancies (Cortes et al., 2015; Lee et al., 2020). Therefore, it would be interesting to compare this molecule with YB-0158 at the structural and functional levels. Conversely, it would be interesting to investigate the impact of UCS15A on tumor-initiating function of CRC tumor samples and to delineate potential similarities with the transcriptional response to peptidomimetics observed in this study. Although PRI-724 showed a high predicted Sam68-binding affinity, it also displayed a poor cancer-selective toxicity index compared with normal intestinal cells and an EC_{50} similar to CWP232228 on HT29 cells. It is plausible that other structural variations in PRI-724 versus CWP232228, e.g., the absence of a 2-propynyl group in position A (Figure 2C, Table S2), which is also absent in ICG-001, could mitigate its cellular uptake and/or bioactivity.

We established several parallels between YB-0158 and other β-turn peptidomimetics at the mechanistic level, including shared capacities to disrupt Sam68-Src interactions, to induce Sam68 nuclear accumulation, to sequester CBP from target genes, and to generate comparable transcriptional responses in CRC cells. Altogether, these observations support our *in silico* modeling approach to identify small molecule structures potentially mimicking UCS15A effect on Sam68's P3-P5 proline-rich domain and its interaction with Src SH3 motif. Previous studies demonstrated that high Sam68 cytoplasmic localization in tumors was significantly associated with poor survival (Zhang et al., 2009), where it can serve as an adaptor protein to modulate Src activity (Huot et al., 2009). Moreover, PRMT1-dependent asymmetric arginine di-methylation of Sam68 R304 residue (within P3 proline-rich region) was previously shown to enhance its nuclear localization in ES cells (Côté et al., 2003), and our data demonstrated that PRMT1 inhibition is impeding Sam68 nuclear accumulation elicited by YB-0158 treatment. Considering the adjacent G305 as a critical residue for YB-0158 binding, it is possible that peptidomimetic-based disruption of Sam68/Src complexes facilitate or mimic the action of PRMT1, contributing to Sam68 nuclear shuttling and Sam68's sequestering effect on CBP. Additional investigations on the relevance of Sam68's R304/G305 motif in meditating the effect of YB-0158 in cancer cells will be necessary to strengthen our understanding of the mechanism of action of β-turn peptidomimetics.

Considering the phenotypic approach originally used to identify ICG-001 and CWP232228 (i.e., TOPFlash luciferase assay), as well as the emerging knowledge on Sam68 vis-a-vis CBP/beta-Catenin, we cannot rule

out the possibility that such molecules were discovered based on direct interactions with Sam68 (Emami et al., 2004; Jang et al., 2015). Although β-turn peptidomimetics were initially characterized as inhibitors of canonical Wnt target genes, our results point toward a broader impact of such small molecules on pathways downstream of CBP. As a transcriptional coactivator, CBP was shown to cooperate with several other transcriptional complexes, such as NF-KB, PU.1, RAR/RXR nuclear receptors, and MYB (Hong et al., 2002a; Kamei et al., 1996; Ramaswamy et al., 2018; Zhong et al., 2002). Overall, YB-0158 yielded a clear transcriptional response supporting impaired self-renewal capacity in CSC populations, which was further confirmed at the functional level *in vivo*. This included a significant inverse relationship between YB-0158-dependent gene modulation in human CRC cells and self-renewal, pluripotency, and EMT-related transcriptional signatures (Figures 4G and S4D). Such a signature likely depends on the downregulation of Wnt/beta-Catenin transcriptional activity, but other downstream pathways of Sam68, including NF-kB, may represent important contributors.

Our work uncovers key insights into the mechanism of action of reverse-turn peptidomimetics in colorectal cancer cells, where Sam68 represents a direct target protein mediating drug-specific response. Using Sam68 binding as a principal criterion to identify and design reverse-turn peptidomimetics with enhanced therapeutic potential, we found YB-0158 as a clinically appealing candidate to target colorectal CSCs in primary patient samples and within *in vivo* systems.

Limitation of the study

The identification of YB-0158 as a β-turn peptidomimetic with CSC-antagonizing functions originates from molecular docking predictions using a 3D protein model generated *in silico*. Although we applied standard methods to estimate the quality of the Sam68 275-374 fragment generated for our virtual chemical screening, it is noteworthy that molecular modeling can be inaccurate or simply erroneous. Thus, in the absence of authentic high-resolution crystal structures, *in silico* modeling observations must be cautiously supported by biological data. Such a caveat in our study was addressed by overexpression experiments where a G305N mutation in Sam68 reduced the biological response to YB-0158 in CRC cells (Figure 3I). Still, a crystal structure of Sam68 bound to the hydrolyzed form of YB-0158 (YB-0159) would strengthen the notion of a direct interaction occurring between the β-turn peptidomimetic small molecule and Sam68 proline-rich domains. Moreover, we did not confirm physical binding of YB-0159 to Sam68 in competitive pull-down assays, as for CWP231904. However, we consider the high similarity between YB-0158 and CWP232228 molecular structures (Tanimoto coefficient: 0.96, Table S1), Sam68 modulation (Figures 3C and 3D), and global transcriptional responses (Figures 4C–4F, S4A, and S4B) are strongly supportive of a common mechanism of action in CRC.

Although other groups reported significant decreases in primary tumor growth upon CWP232228 treatments *in vivo*, we did not observe such an effect using CWP232228 and YB-0158 in our experimental system (Figure 5E). However, it is noteworthy that previous reports on CWP232228 *in vivo* treatments of solid tumors and observations were executed for longer periods (>21 days following the initiation of the treatments) (Jang et al., 2015; Kim et al., 2016, 2019). Considering the effects of YB-0158 observed on primary series of patient-derived organoids (Figure 5C), it is reasonable to think that we would observe reduced primary tumor burden if treatments and measurements would span over longer periods of time. In addition, our *in vivo* analyses were based on a single dosage of CWP232228 and YB-0158 (100 mg/kg), which is based on previous studies on CWP232228, and representing half of its maximum tolerable dose in mice (Benoit et al., 2017; Jang et al., 2015; Kim et al., 2016, 2019). Therefore, it is currently impossible to determine whether lower doses of YB-0158 might be effective to reduce CSC activity *in vivo*, which would constitute critical information for future translational development of this compound. Furthermore, pharmacokinetic experiments showed the disappearance of CWP232228 from mouse plasma by 4 h post injection. With this study, we are not providing specific pharmacokinetic data for YB-0158. Additional investigations in that sense will be essential for future clinical applications.

STAR★METHODS

Detailed methods are provided in the online version of this paper and include the following:

- KEY RESOURCES TABLE
- RESOURCE AVAILABILITY
  - Lead contact
  - Materials availability

- Data and code availability
- EXPERIMENTAL MODEL AND SUBJECT DETAILS
  - Pluripotent stem cell culture
  - HT29 cell culture
  - HCT116 cell culture
  - SW480 cell culture
  - HIEC cell culture
  - MC38 cell culture
  - 293-FT cell culture
  - Primary patient samples
- METHOD DETAILS
  - Key reagents synthesis
  - Western blot analysis
  - Cell growth rate assessment
  - Immunofluorescence analysis
  - Early endoderm differentiation assay
  - Bead conjugation and affinity pulldown experiments
  - In silico modeling analysis
  - Lentiviral-based knockdown and overexpression
  - Co-immunoprecipitation assay
  - Chromatin immunoprecipitation (ChIP) assay
  - Quantitative PCR analysis and transcriptome profiling
  - EdU incorporation assays
  - Apoptosis detection assay
  - Serial organoid formation assay
  - Serial *in vivo* tumor transplantation assay
- QUANTIFICATION AND STATISTICAL ANALYSIS

SUPPLEMENTAL INFORMATION

Supplemental information can be found online at https://doi.org/10.1016/j.isci.2021.103442.

ACKNOWLEDGMENTS

This work was supported by grants from the Cancer Research Society (#22778 and #24039), the Ontario Ministry of Research, Innovation and Science (ER17-13-012), the CIHR (PJT-173541), and the National Science and Engineering Research Council (RGPIN-2018-06521 and DGECR-2018-00029). The authors would like to thank Drs. André Beauchemin (University of Ottawa), Jean-François Beaulieu (Université de Sherbrooke), Mickie Bhatia (McMaster University), Rebecca Auer (The Ottawa Hospital), Jocelyn Côté (University of Ottawa), Catherine O'Brien (Toronto General Hospital/Research Institute), and Christopher Porter and Gareth Palidwor (the Ottawa Bioinformatics Core Facility, OHRI). Graphic abstract and elements of Figures 2A, 3I, 5A, and 5D were created with BioRender.com.

AUTHOR CONTRIBUTIONS

A.N.M. designed and performed experiments, analyzed/interpreted data, and wrote the manuscript; C.J.B. and J.R.H designed and performed experiments and wrote the manuscript; A.Z. performed experiments and analyzed data; M.S.S. and F.M.D. performed *in silico* analysis and contributed to figures design; T.S., A.M.d.S., and A.F.M. performed experiments; Y.D.B. supervised the project, designed experiments, performed experiments, provided results interpretation, and wrote the manuscript.

DECLARATION OF INTERESTS

The authors declare no competing financial interests.

Received: July 28, 2021
Revised: October 9, 2021
Accepted: November 10, 2021
Published: December 17, 2021

REFERENCES

Anderson, R.J., Weng, Z., Campbell, R.K., and Jiang, X. (2005). Main-chain conformational tendencies of amino acids. Proteins *60*, 679–689. https://doi.org/10.1002/prot.20530.

Arensman, M.D., Telesca, D., Lay, A.R., Kershaw, K.M., Wu, N., Donahue, T.R., and Dawson, D.W. (2014). The CREB-binding protein inhibitor ICG-001 suppresses pancreatic cancer growth. Mol. Cancer Ther. *13*, 2303–2314. https://doi.org/10.1158/1535-7163.MCT-13-1005.

Ben-Porath, I., Thomson, M.W., Carey, V.J., Ge, R., Bell, G.W., Regev, A., and Weinberg, R.A. (2008). An embryonic stem cell-like gene expression signature in poorly differentiated aggressive human tumors. Nat. Genet. *40*, 499–507. https://doi.org/10.1038/ng.127.

Benoit, Y.D., Guezguez, B., Boyd, A.L., and Bhatia, M. (2014). Molecular pathways: epigenetic modulation of Wnt-glycogen synthase kinase-3 signaling to target human cancer stem cells. Clin. Cancer Res. *20*, 5372–5378. https://doi.org/10.1158/1078-0432.CCR-13-2491.

Benoit, Y.D., Lepage, M.B., Khalfaoui, T., Tremblay, E., Basora, N., Carrier, J.C., Gudas, L.J., and Beaulieu, J.F. (2012). Polycomb repressive complex 2 impedes intestinal cell terminal differentiation. J. Cell Sci. *125*, 3454–3463. https://doi.org/10.1242/jcs.102061.

Benoit, Y.D., Mitchell, R.R., Risueño, R.M., Orlando, L., Tanasijevic, B., Boyd, A.L., Aslostovar, L., Salci, K.R., Shapovalova, Z., Russell, J., et al. (2017). Sam68 allows selective targeting of human cancer stem cells. Cell Chem. Biol. *24*, 833–844.e9. https://doi.org/10.1016/j.chembiol.2017.05.026.

Benoit, Y.D., Mitchell, R.R., Wang, W., Orlando, L., Boyd, A.L., Tanasijevic, B., Aslostovar, L., Shapovalova, Z., Doyle, M., Bergin, C.J., et al. (2021). Targeting SUMOylation dependency in human cancer stem cells through a unique SAE2 motif revealed by chemical genomics. Cell Chem. Biol. *28*, 1394–1406.e10. https://doi.org/10.1016/j.chembiol.2021.04.014.

Benoit, Y.D., Pare, F., Francoeur, C., Jean, D., Tremblay, E., Boudreau, F., Escaffit, F., and Beaulieu, J.F. (2010). Cooperation between HNF-1alpha, Cdx2, and GATA-4 in initiating an enterocytic differentiation program in a normal human intestinal epithelial progenitor cell line. Am. J. Physiol. Gastrointest. Liver Physiol. *298*, G504–G517. https://doi.org/10.1152/ajpgi.00265.2009.

Bergin, C.J., Zouggar, A., Haebe, J.R., Masibag, A.N., Desrochers, F.M., Reilley, S.Y., Agrawal, G., and Benoit, Y.D. (2021). G9a controls pluripotent-like identity and tumor-initiating function in human colorectal cancer. Oncogene *40*, 1191–1202. https://doi.org/10.1038/s41388-020-01591-7.

Bowers, E.M., Yan, G., Mukherjee, C., Orry, A., Wang, L., Holbert, M.A., Crump, N.T., Hazzalin, C.A., Liszczak, G., Yuan, H., et al. (2010). Virtual ligand screening of the p300/CBP histone acetyltransferase: identification of a selective small molecule inhibitor. Chem. Biol. *17*, 471–482. https://doi.org/10.1016/j.chembiol.2010.03.006.

Boyd, A.L., Aslostovar, L., Reid, J., Ye, W., Tanasijevic, B., Porras, D.P., Shapovalova, Z., Almakadi, M., Foley, R., Leber, B., et al. (2018). Identification of chemotherapy-induced leukemic-regenerating cells reveals a transient vulnerability of human AML recurrence. Cancer Cell *34*, 483–498.e5. https://doi.org/10.1016/j.ccell.2018.08.007.

Chan, K.C., Chan, L.S., Ip, J.C., Lo, C., Yip, T.T., Ngan, R.K., Wong, R.N., Lo, K.W., Ng, W.T., Lee, A.W., et al. (2015). Therapeutic targeting of CBP/β-catenin signaling reduces cancer stem-like population and synergistically suppresses growth of EBV-positive nasopharyngeal carcinoma cells with cisplatin. Sci. Rep. *5*, 9979. https://doi.org/10.1038/srep09979.

Chen, S., Zhou, Y., Chen, Y., and Gu, J. (2018). fastp: an ultra-fast all-in-one FASTQ preprocessor. Bioinformatics *34*, i884–i890. https://doi.org/10.1093/bioinformatics/bty560.

Conery, A.R., Centore, R.C., Neiss, A., Keller, P.J., Joshi, S., Spillane, K.L., Sandy, P., Hatton, C., Pardo, E., Zawadzke, L., et al. (2016). Bromodomain inhibition of the transcriptional coactivators CBP/EP300 as a therapeutic strategy to target the IRF4 network in multiple myeloma. Elife *5*. https://doi.org/10.7554/eLife.10483.

Cortes, J.E., Faderl, S., Pagel, J., Jung, C.W., Yoon, S.-S., Koh, Y., Pardanani, A.D., Hauptschein, R.S., Lee, K.-J., and Lee, J.-H. (2015). Phase 1 study of CWP232291 in relapsed/refractory acute myeloid leukemia (AML) and myelodysplastic syndrome (MDS). J. Clin. Oncol. *33*, 7044. https://doi.org/10.1200/jco.2015.33.15_suppl.7044.

Crespo, M., Vilar, E., Tsai, S.Y., Chang, K., Amin, S., Srinivasan, T., Zhang, T., Pipalia, N.H., Chen, H.J., Witherspoon, M., et al. (2017). Colonic organoids derived from human induced pluripotent stem cells for modeling colorectal cancer and drug testing. Nat. Med. *23*, 878–884. https://doi.org/10.1038/nm.4355.

Côté, J., Boisvert, F.M., Boulanger, M.C., Bedford, M.T., and Richard, S. (2003). Sam68 RNA binding protein is an in vivo substrate for protein arginine N-methyltransferase 1. Mol. Biol. Cell *14*, 274–287. https://doi.org/10.1091/mbc.E02-08-0484.

Dallakyan, S., and Olson, A.J. (2015). Small-molecule library screening by docking with PyRx. Methods Mol. Biol. *1263*, 243–250. https://doi.org/10.1007/978-1-4939-2269-7_19.

Dawood, S., Austin, L., and Cristofanilli, M. (2014). Cancer stem cells: implications for cancer therapy. Oncology (Williston Park) *28*, 1101–1107, 1110.

Eguchi, M., Nguyen, C., Lee, S.C., and Kahn, M. (2005). ICG-001, a novel small molecule regulator of TCF/beta-catenin transcription. Med. Chem. *1*, 467–472. https://doi.org/10.2174/1573406054864098.

Emami, K.H., Nguyen, C., Ma, H., Kim, D.H., Jeong, K.W., Eguchi, M., Moon, R.T., Teo, J.L., Oh, S.W., Kim, H.Y., et al. (2004). A small molecule inhibitor of beta-catenin/CREB-binding protein transcription [corrected]. Proc. Natl. Acad. Sci. U S A *101*, 12682–12687. https://doi.org/10.1073/pnas.0404875101.

Fu, K., Sun, X., Wier, E.M., Hodgson, A., Liu, Y., Sears, C.L., and Wan, F. (2016). Sam68/KHDRBS1 is critical for colon tumorigenesis by regulating genotoxic stress-induced NF-κB activation. Elife *5*. https://doi.org/10.7554/eLife.15018.

Hatano, Y., Fukuda, S., Hisamatsu, K., Hirata, A., Hara, A., and Tomita, H. (2017). Multifaceted interpretation of colon cancer stem cells. Int. J. Mol. Sci. *18*. https://doi.org/10.3390/ijms18071446.

Hong, W., Kim, A.Y., Ky, S., Rakowski, C., Seo, S.B., Chakravarti, D., Atchison, M., and Blobel, G.A. (2002a). Inhibition of CBP-mediated protein acetylation by the Ets family oncoprotein PU.1. Mol. Cell Biol. *22*, 3729–3743. https://doi.org/10.1128/mcb.22.11.3729-3743.2002.

Hong, W., Resnick, R.J., Rakowski, C., Shalloway, D., Taylor, S.J., and Blobel, G.A. (2002b). Physical and functional interaction between the transcriptional cofactor CBP and the KH domain protein Sam68. Mol. Cancer Res. *1*, 48–55.

Huot, M.E., Brown, C.M., Lamarche-Vane, N., and Richard, S. (2009). An adaptor role for cytoplasmic Sam68 in modulating Src activity during cell polarization. Mol. Cell Biol. *29*, 1933–1943. https://doi.org/10.1128/MCB.01707-08.

Jang, G.B., Hong, I.S., Kim, R.J., Lee, S.Y., Park, S.J., Lee, E.S., Park, J.H., Yun, C.H., Chung, J.U., Lee, K.J., et al. (2015). Wnt/β-Catenin small-molecule inhibitor CWP232228 preferentially inhibits the growth of breast cancer stem-like cells. Cancer Res. *75*, 1691–1702. https://doi.org/10.1158/0008-5472.CAN-14-2041.

Jinushi, M., Chiba, S., Yoshiyama, H., Masutomi, K., Kinoshita, I., Dosaka-Akita, H., Yagita, H., Takaoka, A., and Tahara, H. (2011). Tumor-associated macrophages regulate tumorigenicity and anticancer drug responses of cancer stem/initiating cells. Proc. Natl. Acad. Sci. U S A *108*, 12425. https://doi.org/10.1073/pnas.1106645108.

Kamei, Y., Xu, L., Heinzel, T., Torchia, J., Kurokawa, R., Gloss, B., Lin, S.C., Heyman, R.A., Rose, D.W., Glass, C.K., and Rosenfeld, M.G. (1996). A CBP integrator complex mediates transcriptional activation and AP-1 inhibition by nuclear receptors. Cell *85*, 403–414. https://doi.org/10.1016/s0092-8674(00)81118-6.

Kim, J.Y., Lee, H.Y., Park, K.K., Choi, Y.K., Nam, J.S., and Hong, I.S. (2016). CWP232228 targets liver cancer stem cells through Wnt/β-catenin signaling: a novel therapeutic approach for liver cancer treatment. Oncotarget *7*, 20395–20409. https://doi.org/10.18632/oncotarget.7954.

Kim, J.Y., Park, G., Krishnan, M., Ha, E., and Chun, K.S. (2019). Selective Wnt/β-catenin small-molecule inhibitor CWP232228 impairs tumor growth of colon cancer. Anticancer Res. *39*, 3661–3667. https://doi.org/10.21873/anticanres.13514.

Ko, A.H., Chiorean, E.G., Kwak, E.L., Lenz, H.-J., Nadler, P.I., Wood, D.L., Fujimori, M., Inada, T., Kouji, H., and McWilliams, R.R. (2016). Final results of a phase Ib dose-escalation study of PRI-724, a CBP/beta-catenin modulator, plus gemcitabine (GEM) in patients with advanced

pancreatic adenocarcinoma (APC) as second-line therapy after FOLFIRINOX or FOLFOX. J. Clin. Oncol. *34*, e15721. https://doi.org/10.1200/JCO.2016.34.15_suppl.e15721.

Kreso, A., and Dick, J.E. (2014). Evolution of the cancer stem cell model. Cell Stem Cell *14*, 275–291. https://doi.org/10.1016/j.stem.2014.02.006.

Kreso, A., and O'Brien, C.A. (2008). Colon cancer stem cells. Curr. Protoc. Stem Cell Biol. *3*, Unit 3.1. https://doi.org/10.1002/9780470151808.sc0301s7.

Kreso, A., van Galen, P., Pedley, N.M., Lima-Fernandes, E., Frelin, C., Davis, T., Cao, L., Baiazitov, R., Du, W., Sydorenko, N., et al. (2014). Self-renewal as a therapeutic target in human colorectal cancer. Nat. Med. *20*, 29–36. https://doi.org/10.1038/nm.3418.

Lee, J.H., Faderl, S., Pagel, J.M., Jung, C.W., Yoon, S.S., Pardanani, A.D., Becker, P.S., Lee, H., Choi, J., Lee, K., et al. (2020). Phase 1 study of CWP232291 in patients with relapsed or refractory acute myeloid leukemia and myelodysplastic syndrome. Blood Adv. *4*, 2032–2043. https://doi.org/10.1182/bloodadvances.2019000757.

Lepage, M., Seltana, A., Thibault, M.P., Tremblay, É., and Beaulieu, J.F. (2018). Knockdown of laminin α5 stimulates intestinal cell differentiation. Biochem. Biophys. Res. Commun. *495*, 1510–1515. https://doi.org/10.1016/j.bbrc.2017.11.181.

Li, J., Sutter, C., Parker, D.S., Blauwkamp, T., Fang, M., and Cadigan, K.M. (2007). CBP/p300 are bimodal regulators of Wnt signaling. EMBO J. *26*, 2284–2294. https://doi.org/10.1038/sj.emboj.7601667.

Lima-Fernandes, E., Murison, A., da Silva Medina, T., Wang, Y., Ma, A., Leung, C., Luciani, G.M., Haynes, J., Pollett, A., Zeller, C., et al. (2019). Targeting bivalency de-represses Indian Hedgehog and inhibits self-renewal of colorectal cancer-initiating cells. Nat. Commun. *10*, 1436. https://doi.org/10.1038/s41467-019-09309-4.

Love, M.I., Huber, W., and Anders, S. (2014). Moderated estimation of fold change and dispersion for RNA-seq data with DESeq2. Genome Biol. *15*, 550. https://doi.org/10.1186/s13059-014-0550-8.

O'Brien, C.A., Pollett, A., Gallinger, S., and Dick, J.E. (2007). A human colon cancer cell capable of initiating tumour growth in immunodeficient mice. Nature *445*, 106–110. https://doi.org/10.1038/nature05372.

Oneyama, C., Nakano, H., and Sharma, S.V. (2002). UCS15A, a novel small molecule, SH3 domain-mediated protein-protein interaction blocking drug. Oncogene *21*, 2037–2050. https://doi.org/10.1038/sj.onc.1205271.

Patro, R., Duggal, G., Love, M.I., Irizarry, R.A., and Kingsford, C. (2017). Salmon provides fast and bias-aware quantification of transcript expression. Nat. Methods *14*, 417–419. https://doi.org/10.1038/nmeth.4197.

Pfaffl, M.W. (2001). A new mathematical model for relative quantification in real-time RT-PCR. Nucleic Acids Res. *29*, e45. https://doi.org/10.1093/nar/29.9.e45.

Ramaswamy, K., Forbes, L., Minuesa, G., Gindin, T., Brown, F., Kharas, M.G., Krivtsov, A.V., Armstrong, S.A., Still, E., de Stanchina, E., et al. (2018). Peptidomimetic blockade of MYB in acute myeloid leukemia. Nat. Commun. *9*, 110. https://doi.org/10.1038/s41467-017-02618-6.

Sachlos, E., Risueno, R.M., Laronde, S., Shapovalova, Z., Lee, J.H., Russell, J., Malig, M., McNicol, J.D., Fiebig-Comyn, A., Graham, M., et al. (2012). Identification of drugs including a dopamine receptor antagonist that selectively target cancer stem cells. Cell *149*, 1284–1297. https://doi.org/10.1016/j.cell.2012.03.049.

Sharma, S.V., Oneyama, C., Yamashita, Y., Nakano, H., Sugawara, K., Hamada, M., Kosaka, N., and Tamaoki, T. (2001). UCS15A, a non-kinase inhibitor of Src signal transduction. Oncogene *20*, 2068–2079. https://doi.org/10.1038/sj.onc.1204296.

Soneson, C., Love, M.I., and Robinson, M.D. (2015). Differential analyses for RNA-seq: transcript-level estimates improve gene-level inferences. F1000Res *4*, 1521. https://doi.org/10.12688/f1000research.7563.2.

Studer, G., Rempfer, C., Waterhouse, A.M., Gumienny, R., Haas, J., and Schwede, T. (2020). QMEANDisCo-distance constraints applied on model quality estimation. Bioinformatics *36*, 1765–1771. https://doi.org/10.1093/bioinformatics/btz828.

Subramanian, A., Tamayo, P., Mootha, V.K., Mukherjee, S., Ebert, B.L., Gillette, M.A., Paulovich, A., Pomeroy, S.L., Golub, T.R., Lander, E.S., and Mesirov, J.P. (2005). Gene set enrichment analysis: a knowledge-based approach for interpreting genome-wide expression profiles. Proc. Natl. Acad. Sci. U S A *102*, 15545–15550. https://doi.org/10.1073/pnas.0506580102.

Tang, Z., Kang, B., Li, C., Chen, T., and Zhang, Z. (2019). GEPIA2: an enhanced web server for large-scale expression profiling and interactive analysis. Nucleic Acids Res. *47*, W556–W560. https://doi.org/10.1093/nar/gkz430.

Tokunaga, Y., Osawa, Y., Ohtsuki, T., Hayashi, Y., Yamaji, K., Yamane, D., Hara, M., Munekata, K., Tsukiyama-Kohara, K., Hishima, T., et al. (2017). Selective inhibitor of Wnt/β-catenin/CBP signaling ameliorates hepatitis C virus-induced liver fibrosis in mouse model. Sci. Rep. *7*, 325. https://doi.org/10.1038/s41598-017-00282-w.

Tuveson, D., and Clevers, H. (2019). Cancer modeling meets human organoid technology. Science *364*, 952–955. https://doi.org/10.1126/science.aaw6985.

Vogt, M., and Bajorath, J. (2020). Ccbmlib - a python package for modeling Tanimoto similarity value distributions. F1000Res. *9*. https://doi.org/10.12688/f1000research.22292.2.

Wainwright, E.N., and Scaffidi, P. (2017). Epigenetics and cancer stem cells: unleashing, hijacking, and restricting cellular plasticity. Trends Cancer *3*, 372–386. https://doi.org/10.1016/j.trecan.2017.04.004.

Werbowetski-Ogilvie, T.E., Bosse, M., Stewart, M., Schnerch, A., Ramos-Mejia, V., Rouleau, A., Wynder, T., Smith, M.J., Dingwall, S., Carter, T., et al. (2009). Characterization of human embryonic stem cells with features of neoplastic progression. Nat. Biotechnol. *27*, 91–97. https://doi.org/10.1038/nbt.1516.

Wörthmüller, J., and Rüegg, C. (2020). The crosstalk between FAK and Wnt signaling pathways in cancer and its therapeutic implication. Int. J. Mol. Sci. *21*. https://doi.org/10.3390/ijms21239107.

Zhang, Z., Li, J., Zheng, H., Yu, C., Chen, J., Liu, Z., Li, M., Zeng, M., Zhou, F., and Song, L.B. (2009). Expression and cytoplasmic localization of SAM68 is a significant and independent prognostic marker for renal cell carcinoma. Cancer Epidemiol. Biomarkers Prev. *18*, 2685–2693. https://doi.org/10.1158/1055-9965.EPI-09-0097.

Zhong, H., May, M.J., Jimi, E., and Ghosh, S. (2002). The phosphorylation status of nuclear NF-kappa B determines its association with CBP/p300 or HDAC-1. Mol. Cell *9*, 625–636. https://doi.org/10.1016/s1097-2765(02)00477-x.

Zhou, H., Cao, H., and Skolnick, J. (2018). FINDSITE. J. Chem. Inf. Model. *58*, 2343–2354. https://doi.org/10.1021/acs.jcim.8b00309.

Zhou, H., and Skolnick, J. (2012). Template-based protein structure modeling using TASSER(VMT.). Proteins *80*, 352–361. https://doi.org/10.1002/prot.23183.

Zhu, A., Ibrahim, J.G., and Love, M.I. (2019). Heavy-tailed prior distributions for sequence count data: removing the noise and preserving large differences. Bioinformatics *35*, 2084–2092. https://doi.org/10.1093/bioinformatics/bty895.

STAR★METHODS

KEY RESOURCES TABLE

REAGENT or RESOURCE	SOURCE	IDENTIFIER
Antibodies		
Anti-acetyl-Histone H3 (Lys14) antibody	Millipore	Cat# 07-353; RRID: AB_310545
Histone H3 (acetyl K18) antibody [EP959Y]	Abcam	Cat# ab40888; RRID: AB_732923
Histone H3 antibody	Abcam	Cat# ab1791; RRID: AB_302613
Anti-GAPDH antibody [6C5]	Abcam	Cat# ab8245; RRID: AB_2107448
CBP Polyclonal Antibody	ThermoFisher	Cat# PA5-27369; RRID: AB_2544845
Anti-Sam68 antibody	Millipore	Cat# 07-415; RRID: AB_310597
Anti-Human Hnf-3 beta / foxa2 Polyclonal antibody	R&D Systems	Cat# AF2400; RRID: AB_2294104
Oct-4A (C30A3) Rabbit mAb	Cell Signaling	Cat# 2840; RRID: AB_2167691
Mouse Anti-Catenin, beta Monoclonal Antibody	BD Biosciences	Cat# 610154; RRID: AB_397555
Anti-Myb, clone 1-1 antibody	Millipore	Cat# 05-175; RRID: AB_2148022
Anti-ETS2 antibody [OTI1H4]	Cell Signaling	Cat# 9542; RRID: AB_2160739
GATA2 antibody - ChIP Grade	Abcam	Cat# ab22849; RRID: AB_447334
Anti-PTMA antibody	Abcam	Cat# ab208929; RRID: N/A
Anti-v-Src (Ab-1) Mouse mAb (327) antibody	Millipore	Cat# OP07-100UG; RRID: AB_564508
Phospho-Src Family (Tyr416) (D49G4) Rabbit mAb antibody	Cell Signaling	Cat# 6943; RRID: AB_10013641
Anti-Asymmetric Di-Methyl Arginine Motif [adme-R], Rabbit mAb mix	Cell Signaling	Cat# 13522S; RRID: AB_2665370
Anti-Active-beta-Catenin (anti-ABC), clone 8E7 antibody	Millipore	Cat# 05-665; RRID: AB_309887
Anti-Actin Antibody, clone C4	Millipore	Cat# MAB1501; RRID: AB_2223041
E-Cadherin (24E10) Rabbit mAb antibody	Cell Signaling	Cat# 3195; RRID: AB_2291471
Mouse Anti-Human Alpha-smooth muscle actin Monoclonal antibody	R&D Systems	Cat# MAB1420; RRID: AB_262054
Mouse Anti-Ki-67 Monoclonal Antibody	BD Biosciences	Cat# 556003; RRID: AB_396287
Biological samples		
CRC patient sample	(Bergin et al., 2021)	#92
CRC patient sample	(Bergin et al., 2021)	#146
CRC patient sample	(Bergin et al., 2021)	#162
Chemicals, peptides, and recombinant proteins		
CWP232228	Otava Chemicals Ltd.	N/A
C646	Tocris	Cat# 42-001-0
I-CBP112 (hydrochloride)	Cayman Chemical	Cat# 14468-1
ICG-001	Selleck Chemicals	Cat# S2662
CHIR 99021	Tocris	Cat# 4423
PRI-724	Tocris	Cat# 6326
YB-0158	Haoyuan Chemexpress	N/A
Furamidine (hydrochloride)	Cayman Chemical	Cat# 19121
Human/Murine/Rat Activin A	PeproTech	Cat# 120-14E
Recombinant Human HGF (Insect derived)	PeproTech	Cat# 100-39
Staurosporine	Tocris	Cat# 1285

(*Continued on next page*)

Continued

REAGENT or RESOURCE	SOURCE	IDENTIFIER
IRDYE 800CW 2DG optical probe	LI-COR, Inc.	Cat# 926-08946
mTeSR™1	STEMCELL Technologies	Cat# 85850
Corning™ Matrigel™ Membrane Matrix	Fisher Scientific	Cat# CB-40234
FBS fetal bovine serum	Thermo Fisher	Cat# 12483-020
Critical commercial assays		
Dynabeads Protein G for Immunoprecipitation	Thermo Fisher	Cat# 10003D
Dynabeads M-270 for affinity pulldowns	ThermoFisher	Cat# 14307D
EdU Staining Proliferation Kit (iFluor 647)	Abcam	Cat# ab222421
CellEvent™ Caspase-3/7 Green Detection Reagent	Thermo Fisher	Cat# C10423
Chromatin IP DNA Purification kit	Active Motif, Inc.	Cat# 58002
Fixation/Permeabilization Solution Kit	BD Bioscience	Cat# 554714
PowerUp™ SYBR™ Green Master Mix	Thermo Fisher	Cat# A25742
SuperScript VILO cDNA Synthesis Kit	Thermo Fisher	Cat# 11754050
Total RNA Purification Kit	Norgen Biotek Corp.	Cat# 37500
Immobilon Western Chemiluminescent HRP Substrate	Millipore	WBKLS0500
Deposited data		
RNA sequencing data: YB-0158, ICG-001, and CWP232228 (vs. DMSO) treatments in HT29 cells	This paper	GSE176026
Peptidomimetic analog structures	Patent: Reverse-turn mimetics and method relating thereto	US8101751B2
Human Sam68, isoform-1 (*KHDRBS1*) amino acid sequence	Uniprot	Q07666-1
Human wt Sam68 275-374 peptide structural model	This paper	https://modelarchive.org/doi/10.5452/ma-lnvcb
Human G305A Sam68 275-374 peptide structural model	This paper	https://modelarchive.org/doi/10.5452/ma-i6w0x
Human G305N Sam68 275-374 peptide structural model	This paper	https://modelarchive.org/doi/10.5452/ma-eal5i
Human G305S Sam68 275-374 peptide structural model	This paper	https://modelarchive.org/doi/10.5452/ma-rn6yg
Gene expression signatures for GSEAs	This paper, Table S4	N/A
Experimental models: Cell lines		
H9 PSCs	Wicell	N/A
Transformed H9 PSCs	M.Bhatia lab	PMID:19122652
HT29	ATCC®	HTB-38™
HCT116	ATCC®	CCL-247™
SW480	ATCC®	CCL-228™
HIEC	J-F Beaulieu lab	PMID: 8612712
MC38	Kerafast, Inc.	Cat# ENH204-FP
293FT	Thermo Fisher	Cat#R70007
Recombinant DNA		
pLKO.1-Non-Mammalian shRNA Control	Millipore Sigma	Cat#SHC002
pLKO.1-sh*KHDRBS1* (NM_006559)	Millipore Sigma	TRCN0000000044

(*Continued on next page*)

Continued

REAGENT or RESOURCE	SOURCE	IDENTIFIER
pLKO.1-sh*KHDRBS1* (NM_006559)	Millipore Sigma	TRCN0000000045
pLKO.1-sh*KHDRBS1* (NM_006559)	Millipore Sigma	TRCN0000000046
pLKO.1-sh*KHDRBS1* (NM_006559)	Millipore Sigma	TRCN0000428752
pLKO.1-sh*KHDRBS1* (NM_006559)	Millipore Sigma	TRCN0000428104
pLKO.1-sh*CREBBP* (NM_004380)	Millipore Sigma	TRCN0000006485
pLKO.1-sh*CREBBP* (NM_004380)	Millipore Sigma	TRCN0000006486
pLKO.1-sh*CREBBP* (NM_004380)	Millipore Sigma	TRCN0000356053
pLKO.1-sh*CREBBP* (NM_004380)	Millipore Sigma	TRCN0000356081
pLKO.1-sh*CREBBP* (NM_004380)	Millipore Sigma	TRCN0000011027
pLKO.1-sh*CREBBP* (NM_004380)	Millipore Sigma	TRCN0000356082
pLenti-C-mGFP-P2A-Puro	OriGene Tech.	Cat#PS100093
pLenti-*KHDRBS1*-C-mGFP-P2A-Puro	Origene Tech.	Cat#RC200263L4
pLenti-*KHDRBS1*-G305N-C-mGFP-P2A-Puro	Origene Tech.	Cat#CW306793
Oligonucleotides		
Human *GAPDH* cDNA primers	Integrated DNA Technologies	Fwd: GAAATCCCATCACCATCTTCCAGG
		Rev: GCAAATGAGCCCCAGCCTTCTC
Human *SOX9* cDNA primers	Integrated DNA Technologies	Fwd: GTACCGCACTTGCACAAC
		Rev: TCTCGCTCTCGTTCAGAAGTC
Human *LGR5* cDNA primers	Integrated DNA Technologies	Fwd: TGCTCTTCACCAACTGCATC
		Rev: CTCAGGCTCACCAGATCCTC
Human *BIRC5* cDNA primers	Integrated DNA Technologies	Fwd: AGGACCACCGCATCTCTACAT
		Rev: AAGTCTGGCTCGTTCTCAGTG
Human *LGR5* ChIP primers	Integrated DNA Technologies	Fwd: GCGATTTCTTTGAGGCTTTG
		Rev: ATCCGAAAGATTGGCATCAC
Human *MYC* ChIP primers	Integrated DNA Technologies	Fwd: AATGCCTTTGGGTGAGGGAC
		Rev: TCCGTGCCTTTTTTTGGGG
Software and algorithms		
CellReporterXpress	Molecular Devices	https://www.moleculardevices.com/products/cellular-imaging-systems/acquisition-and-analysis-software/cellreporterxpress#gref
LigPlot+ (v2.2.4)	EMBL-EBI	https://www.ebi.ac.uk/thornton-srv/software/LigPlus/
Pubchem Sketcher (v2.4)	NCBI	https://pubchem.ncbi.nlm.nih.gov//edit3/index.html
UCFS Chimera (v1.4)	UCSF-RBVI	https://www.cgl.ucsf.edu/chimera/
PyRx (v0.8)	(Dallakyan and Olson, 2015)	https://pyrx.sourceforge.io
Pymol (v.2.4)	Schrödinger	https://pymol.org/2/
RDKit fingerprinting	(Vogt and Bajorath, 2020)	https://www.rdkit.org/docs/GettingStartedInPython.html
TASSER-VMT / FINDSITEComb 2.0	(Zhou et al., 2018; Zhou and Skolnick, 2012)	https://sites.gatech.edu/cssb/findsite-comb-2/
fastp version 0.20.1	(Chen et al., 2018)	https://doi.org/10.1093/bioinformatics/bty560
DESeq2 version 1.30.1	(Love et al., 2014)	https://bioconductor.org/packages/release/bioc/html/DESeq2.html
Pheatmap library version 1.0.12	Kaivo Kolde	https://cran.r-project.org/package=pheatmap

(*Continued on next page*)

Continued

REAGENT or RESOURCE	SOURCE	IDENTIFIER
R VennDiagram package version 1.6.20	Hanbo Chen	https://cran.r-project.org/package=VennDiagram
EnhancedVolcano package	Kevin Blighe, Sharmila Rana, Myles Lewis	https://github.com/kevinblighe/EnhancedVolcano
GEPIA2	(Tang et al., 2019)	http://gepia2.cancer-pku.cn/#index
GSEA software version 4.0.3	(Subramanian et al., 2005)	https://www.gsea-msigdb.org/gsea/index.jsp

RESOURCE AVAILABILITY

Lead contact

Further information and requests for resources and reagents should be directed to the lead contact, Dr. Yannick D. Benoit (ybenoit@uottawa.ca).

Materials availability

Reagents generated in this study are available from the lead contact under Materials Transfer Agreements.

Data and code availability

- RNA sequencing data are publicly available at the Gene Expression Omnibus (GEO) database: GSE176026. Theoretical models of Sam68 structures are publicly available at modelarchive.org.
- This paper does not report original code.
- Any additional information reported in this paper is available from the lead contact upon request.

EXPERIMENTAL MODEL AND SUBJECT DETAILS

Pluripotent stem cell culture

H9 (hPSCs) and transformed H9 (t-hESCs) were cultured on Matrigel-coated (BD Biosciences 353234) tissue culture plates in mTeSR-1 medium (STEMCELL Technologies, #85850) at 37°C 5% CO_2. H9 cell cultures were passaged every 7 days using Collagenase IV 100units/mL (STEMCELL Technologies, #07909) and mechanical scraping of cell clumps, at a ratio of 1:2.5. t-hESCs were passaged every 3 days according to the same method, at a ratio of 1:4 (Werbowetski-Ogilvie et al., 2009).

HT29 cell culture

HT29 (Female) were cultured in McCoy's 5A medium (Gibco) supplemented with 10% FBS (Thermo Fisher) at 37°C 5% CO_2. Original cultures were seeded at 150k cells per well in TC-treated 6-well plates (CellTreat Scientific Products) and passaged every 5 days at a ratio of 1 to 5.

HCT116 cell culture

HCT116 (Male) were cultured in McCoy's 5A medium (Gibco) supplemented with 10% FBS (Thermo Fisher) at 37°C 5% CO_2. Original cultures were seeded at 150k cells per well in TC-treated 6-well plates (CellTreat Scientific Products) and passaged every 5 days at a ratio of 1 to 10.

SW480 cell culture

SW480 (Male) were cultured in Leibovitz's L-15 medium (Gibco) supplemented with 10% FBS (Thermo Fisher) at 37°C 5% CO_2. Original cultures were seeded at 150k cells per well in TC-treated 6-well plates (CellTreat Scientific Products) and passaged every 5 days at a ratio of 1 to 4.

HIEC cell culture

HIEC cells were cultured in OptiMEM medium (Gibco) supplemented with 4% Premium quality FBS (Wisent), 20mM HEPES, 10mM GlutaMAX (Gibco), and 10ng/ml EGF at 37°C 5% CO_2. Original cultures were seeded at 300k cells per well in TC-treated 6-well plates (CellTreat Scientific Products) and passaged every 5 days at a ratio of 1 to 3.

MC38 cell culture

Mouse colorectal adenocarcinoma MC38 (Male) cells were cultured in DMEM medium (Gibco) supplemented with 10% FBS (Thermo Fisher), 2mM glutamine, 0.1mM nonessential amino acids, 1mM sodium pyruvate, and 10mM HEPES at 37°C 5% CO_2. Original cultures were seeded at 150k cells per well in TC-treated 6-well plates (CellTreat Scientific Products) and passaged every 3 days at a ratio of 1 to 5.

293-FT cell culture

293FT cells were cultured in DMEM medium (Gibco) supplemented with 10% FBS (Thermo Fisher), 1mM non-essential amino acids, 1mM L-Glut, 1mM sodium pyruvate at 37°C 5% CO_2. Original cultures were seeded at 500k per 10cm TC-treated petri dishes and passaged every 3 days at a ratio of 1 to 6.

Primary patient samples

Primary colorectal tumor samples were obtained with patient informed consent, as approved by the Ottawa Health Science Network Research Ethics Board (OHSN-REB) via the Global Tissue Consenting initiative (GTC, OHRI), the University Health Network Research Ethics Board, and from Celprogen Inc. (#36112-39P, Torrance, CA). Tumor tissues were mechanically minced and incubated with Collagenase A (3 mg/mL) for 60 min at 37°C and filtered using a 40-μm cell strainer. Red blood cells were removed using ammonium chloride solution (STEMCELL Technologies) (5 min). Isolated cells were maintained as spheroids in ultra-low adhesion flasks with DMEM/F-12 (Gibco) (1:1 ratio) supplemented with penicillin-streptomycin (1%) (Gibco), L-glutamine (2 mM) (Gibco), nonessential amino acids (1X) (Gibco), sodium pyruvate (1 mM) (Gibco), HEPES (Gibco), heparin (4 μg mL−1), B27 supplement (GIBCO), N2 supplement (GIBCO), lipids mixture (Sigma), EGF (20 ng/mL) and bFGF (10 ng/mL) (Kreso and O'Brien, 2008).

METHOD DETAILS

Key reagents synthesis

Small molecule YB-0158 (2H-Pyrazino[2,1-c][1,2,4]triazine-1(6H)-carboxamide, hexahydro-8-(1H-indazol-7-ylmethyl)-4,7- dioxo-N-(phenylmethyl)-6-[[4-(phosphonooxy)phenyl]methyl]-2-(2-propen-1-yl)-, sodium salt (1:2), (6S,9aS)-, PubChem CID 90301078) was synthesized by Haoyuan Chemexpress Co. Ltd. (Shanghai, China), according to patent route WO 2009051399 A2, compound #23 in patent table #2. 1H NMR (CDCl3, 300 MHz): δ 8.08 (s, 1H), δ 7.72 (t, J = 6.0 Hz, 1H), δ 7.34-7.09 (m, 6H), δ 7.00-6.92 (m, 3H), δ 5.56-5.47 (m, IH), δ 5.40–5.36 (m, IH), δ 5.18 (t, J = 6.0 Hz1 IH), δ 4.92–4.57 (m, 5H), δ 4.33–4.14 (m, 2H), δ 3.61–3.48 (m, 2H), δ 3.28–3.14 (m, 5H) is presented in Data S1. CWP232228 was produced by Otava Chemicals Ltd. (Concord, Canada) based on the organic synthesis protocol reported by Benoit et al. (Benoit et al. 2017). 1H-NMR validation (D2O, 300 MHz) was performed by the provider as quality control (Data S1).

Western blot analysis

Western analyses were performed on SDS-PAGE gels under denaturing conditions. Total protein samples were prepared in Laemmli Sample Buffer (60mM Tris-HCL pH 6.8, 2% SDS, 10% glycerol, 5% β-mercaptoethanol, 0.01% bromophenol blue), sonicated and thermo-reduced/denatured (5 min, 95°C) prior to electrophoresis on 12% polyacrylamide gels (Benoit et al., 2010). Membranes were blocked in PBS containing 5% skim milk and 0.1% TWEEN 20. Primary antibodies were diluted in the blocking solution, and incubated overnight at 4°C (key resources table). After 3 sequential washing steps (10 min each) with PBS, membranes were incubated for 1 hour with horseradish peroxidase-conjugated secondary antibodies (Anti-Mouse IgG (H+L), HRP Conjugate, Cat#W4021, and anti-Rabbit IgG (H&L) HRP Conjugate, Cat#W4011, Promega), washed 3 times (10 mins) in PBS-Tween, and developed using the Immobilon Western Kit (Millipore, WBKLS0100). Blot images were acquired using a ChemiDoc™ XRS+ System with Image Lab™ Software (Bio Rad). Quantitative optical densitometry signal analysis was performed using Image J software (National Institutes of Health).

Cell growth rate assessment

Each cell model was plated at a density of $5x10^3$ cells/well in 96-well culture plates, 24h prior to drug treatments. Small molecules ICG-001, CWP232228, PRI-724, I-CBP112, C646, and YB-0158 were used at concentrations ranging from 0.002 to 20μM for 48 hours. Equivalent volumes of vehicle DMSO were used as control (≤0.1%). Cells were formalin-fixed, stained with Hoescht 33342, and plates were imaged with an ImageXpress Pico High-Content imaging system (Molecular Devices). Images were acquired and analyzed

using the CellReporterXpress software, and half maximum effective concentration (EC_{50}) values were calculated using GraphPad Prism.

Immunofluorescence analysis

Formaldehyde-fixed paraffin-embedded mouse ileum tissue sections were rehydrated, quenched in 0.1M glycine buffer, and blocked with a 2.5% BSA-PBS solution prior to immunostaining (Benoit et al., 2010). For staining of cells, human colorectal lines and t-hESCs were plated, cultured, and treated as above described, prior to fixation with 2% formalin and incubated in Perm/Wash buffer (BD Biosciences) at 4°C for 15-30 min. Anti-OCT4, anti-FOXA2, anti-Sam68, anti-E-Cadherin, anti-Ki-67, and anti-Alpha smooth muscle actin primary antibodies (key resources table) were diluted in 1% BSA-PBS solution and incubated overnight at 4°C. Secondary antibodies were used at 1:500 in a 1% BSA-PBS solution. For staining on tissue sections, slides were mounted using Vectashield mounting medium with DAPI (Vector labs). For cell staining, nuclei were stained with Hoechst 33342. Cells and tissue sections were imaged with an ImageXpress Pico High-Content imaging system (Molecular Devices). Images were acquired and analyzed using the CellReporterXpress software.

Early endoderm differentiation assay

t-PSC cells were mechanically dissociated and plated on Matrigel coated 96-well plates, and treated with CWP232228 (0.1μM) or I-CBP112 (0.25μM) in mTeSR-1 media (STEMCELL Technologies) for 48 hours. Control (plain media and DMSO) and treated cells were incubated in endoderm differentiation media (RPMI 1640 supplemented with B-27 additive (Thermo Fisher), 100ng/ml of Activin A (PeproTech), 3uM of CHIR99021 (Tocris), and 100ng/ml of HGF (Peprotech)) over 6 days. Then, cells were fixed and permeabilized (Fixation/Permeabilization Solution Kit, BD Bioscience) and immunostained as described above, using anti-OCT4 and anti-FOXA2 primary antibodies (key resources table). Fluorescence images were acquired and analyzed using an ImageXpress Pico High-Content imaging system (Molecular Devices), as described in the immunofluorescence analysis section.

Bead conjugation and affinity pulldown experiments

CWP232228 was treated by phosphatase to remove the phosphate group and produce its active form CWP231904. Next, CWP231904 was functionalized with a carboxylic group by succinic anhydride with DMAP catalysis. Carboxylic-functionalized CWP231904 was loaded onto amine-functionalized magnetic beads with HATU activation. As a quality control step, amine-functionalized beads and CWP231904-conjugated beads were treated with ammonium hydroxide and the release of CWP231904 was confirmed by MALDI-TOF (Benoit et al., 2021). For affinity pulldown assays, hPSCs were lysed in 1% NP-40 lysis buffer (50 mM Tris-HCL pH 7.4 + protease inhibitor cocktail) and quantified. Suspensions of 0.8mg of total protein content were incubated with CWP231904-conjugated magnetic Dynabeads. Unconjugated magnetic Dynabeads were used as control. 100uM of soluble CWP231904 and ICG-001 were added to the pulldown reactions for competition assays. Samples were incubated for 2h at room temperature under agitation and were washed 3 times using 1% NP-40 lysis buffer + protease inhibitor cocktail. Washed beads were boiled in Laemmli sample buffer at 95°C for 10 min and analyzed by Western blot.

In silico modeling analysis

A structural model of the portion of human Sam68 including residues 275 to 374 (Q07666-1, Sam68 isoform-1) was generated using the TASSER-VMT algorithm, within the FINDSITEComb2.0 server (Zhou et al., 2018; Zhou and Skolnick, 2012). The quality of the model was assessed using the single model composite score QMEAN, including the consensus-based distance constraint (DisCo) score reported by Studer et al. (Studer et al., 2020). A score combination approach was applied using a neural network trained to predict per-residue lDDT scores. The global lDDT score obtained for the P3-P5 Sam68 model is 0.69, which is considered as a "good quality" model (Studer et al., 2020). Ramachandran plot illustrating residue-specific conformation preferences of Φ and Ψ torsion angles in P3-P5 Sam68 model were generated by the Zlab Ramachandran plot server (Anderson et al., 2005). For subsequent molecular docking, the library of small molecule ligands including β-turn peptidomimetics (ICG-001, CWP231904, PRI-724(OH)), 41 distinct structures from patent US8101751B2 presenting either methyl, alkene, and alkyne group in position "A" (Figure 2C) (total of 123 entities), and 19 random drug structures (library size: n=145). Pubchem Sketcher (v2.4) was used to generate simplified molecular-input line-entry system (SMILES) strings, and UCFS Chimera (v1.4) was used to convert the SMILES string into PDB files. The virtual screening software PyRx

(v0.8), running AutoDock Vina and built-in PDBQT converter Open Babel was used to determine docking energy for each ligand from the peptidomimetic library with the Sam68 275-374 model, for a minimum of 3 runs at exhaustiveness ("E") of 8, with a standard deviation limit of 0.1 (for unknown peptidomimetics only), and an RMSD = 0. A total of 89 structures passed such criteria and were presented in Table S1. Molecule similarity scoring vs. CWP231904 was determined using RDKit Fingerprinting (Vogt and Bajorath, 2020) and presented in Table S1. Output files from molecular docking analysis were opened with Pymol software (v.2.4.x) and unique docking conformations for each compound were converted as PDB file and transferred to LigPlot+ (v2.2.4) to be visualized in 2D using standard parameters. Pymol was also used to generate *in silico* mutants of Sam68 275-374 peptide (G305A, G305N, G305S) using its built-in mutagenesis feature, followed by PyRx processing to determine docking energy for a minimum of 3 runs at E=50, RMSD = 0 (Table S2).

Lentiviral-based knockdown and overexpression

Scramble control, *KHDRBS1* (Sam68) and *CREBBP* (CBP) targeting shRNA expression plasmids were purchased at Millipore Sigma (key resources table) and co-transfected with pMD2.G (Addgene #12259) and psPAX2 (Addgene #12260) vectors in 293-FT cells using Lipofectamine 2000 (Thermo Fisher). Lentiviral particles were harvested 24 and 48h post-transfection, where the conditioned medium was collected, centrifuged to remove cells and debris, filtered through a 0.45um filter and then ultracentrifuged at 20K x g for 2hr at 4°. Concentrated lentivirus preps were re-suspended in 0.5ml of PBS per 10cm culture plate of 293-FT cells worth of supernatant. Individual lentivirus preps were titrated on the desired cell line to be transduced in order to optimize expression but minimize transduction induced cell death. Custom mutagenesis of human *KHDRBS1* cDNA and cloning into pLenti-mGFP-P2A-Puro vector was performed by OriGene Technologies, and lentiviral particles for control, wild-type Sam68/*KHDRBS1*, and G305N Sam68/*KHDRBS1* overexpression were generated as above-described. Lentiviral infections were executed on $5x10^5$ cells/well in 6-well plates, incubated with 0.5ml of viral suspension + 8ug/mL of polybrene (Millipore Sigma) for 16 hours. Culture media containing 0.5 μg/ml of puromycin was used for 10 days of selection. Knockdown efficiency and protein overexpression were determined by western blot.

Co-immunoprecipitation assay

HT29 cultures were treated with CWP232228 (1.5μM), YB-0158 (0.3μM), or control DMSO (0.1%) for 48 hours, and washed twice with PBS. Cells were lysed in 1% NP-40 lysis buffer (IP buffer: 50 mM Tris-HCL pH 7.4 + protease inhibitor cocktail). Protein samples were incubated overnight at 4°C with 10ul of Protein G coated magnetic Dynabeads (Invitrogen) bound to 5μg of anti-Sam68 primary antibody or control IgGs (key resources table). Then, beads were washed 3 times (10 mins) with IP buffer. Immunoprecipitated complexes were eluted from beads by boiling with Laemmli sample buffer at 95°C for 10 min and analyzed by Western blot.

Chromatin immunoprecipitation (ChIP) assay

For each ChIP condition, $2x10^6$ HT29 cells were collected and cross-linked using 1% formaldehyde. Chromatin was fragmented by sonication in buffer containing 1% NP-40 and 0.1% SDS to obtain fragments of ~250 bp length. Sonicated DNA was subjected to immunoprecipitation using anti-CBP primary antibody (5μg) (key resources table) conjugated with Dynabeads Protein G (Thermo Fisher). Mouse IgGs (5μg) were used as controls. Immunoprecipitated DNA was reverse cross-linked, purified using Chromatin IP DNA purification kit (Active Motif), and subjected to quantitative PCR analysis to detect *LGR5* and *MYC* promoter fragments. Promoter-specific ChIP primers are listed in key resources table. To calculate relative chromatin enrichment values, PCR signal obtained from specific antibody pulldowns were divided by signal observed from ChIP input material based on a standard curve equation (Benoit et al., 2017).

Quantitative PCR analysis and transcriptome profiling

Total RNA was extracted using the total RNA purification kit by Norgen Biotech Corp, following the manufacturer's guidelines. Purified RNA was quantified using a Nanodrop 2000 spectrophotometer (Thermo Fisher). For quantitative PCR analysis, cDNA was synthesized from 1μg of total RNA using SuperScript VILO cDNA Synthesis Kit (Thermo Fisher). qPCR reactions were carried out using PowerUp SYBR Green Master Mix (Thermo Fisher) per manufacturer's recommendation. Amplification was performed using an ABI 7500 Real-Time PCR System. Primer sequences used in this study are presented in key resources table. All reactions were normalized to GAPDH as reference gene, and relative gene quantification was calibrated

against vehicle/control-treated samples according to a method described by Pfaffl et al. (Pfaffl, 2001). For transcriptome profiling analysis by next-generation RNA sequencing, RNA integrity was evaluated for each RNA sample using a Fragment Analyzer HS NGS assay (AATI). A RNA Quality Number (RQN) of 8.0 or higher was considered satisfactory for library construction. Library construction was performed with a Truseq RNA v2 (Illumina). Libraries were prepared with unique barcodes compatible with the Illumina NextSeq 500 platform. Quantification of the libraries was performed with a Qubit HS DNA assay and library fragment size was evaluated with a Fragment Analyzer HS NGS assay. Libraries were normalized to the same concentration, then samples were pooled in equal amounts. Next-generation RNA sequencing was performed on an Illumina NextSeq 500 platform, according to 1 x 75bp cycles of single-end sequencing, yielding 25 million reads per sample. PhiX ssDNA was spiked in each sample and used as a technical control for clustering reactions. Raw sequence data were processed with fastp v0.20.1 (Chen et al., 2018) to perform automatic adapter trimming and read quality filtering, retaining reads with at least 60% of bases having $Q \geq 15$, and no more than 5 'N' bases. Transcripts were quantified using the Salmon transcript abundance method (v1.3.0) (Patro et al., 2017). Data were loaded into R (v4.0.2) using the tximport library (Soneson et al., 2015), and the gene/count matrix was filtered to retain only genes with five or more mapped reads in two or more samples. Differential expression was assessed using DESeq2 v1.30.1 (Love et al., 2014). Differential gene expression between treatment vs DMSO replicates was calculated using the DESeq2 lfcShrink() function, applying the apeglm method (v 1.12.0) (Zhu et al., 2019). Multiple testing correction was performed using the Benjamini Hochberg method, and lists of significantly DE genes were identified using a q-value (i.e. a corrected p-value) cut-off of 0.05. The hierarchically clustered heatmap was generated with the pheatmap library v1.0.12 (https://cran.r-project.org/package=pheatmap), using the R hclust function for hierarchical clustering. Venn diagrams of overlapping gene sets were generated with the R VennDiagram package (v1.6.20). Volcano plots were generated with the EnhancedVolcano package with points colored relative to a p-value cutoff of 10^{-3} and a log2FoldChange cutoff of log2(2). Gene signature enrichment analysis (GSEA) were performed using GSEA Software version 4.0.3 (Subramanian et al., 2005). Differential gene expression analysis between TCGA COAD and READ tumor and healthy tissues was performed using the Gene Profiling Interactive Analysis GEPIA2 platform (Tang et al., 2019).

EdU incorporation assays

Proliferation rate of HT29 cells was determined using a 5-ethynyl-2'-deoxyuridine (EdU) Staining Proliferation kit (iFluor 647) (Abcam) (Benoit et al., 2021). Briefly, 5,000 cells per well were plated in 96-well plates. 24 hours post-seeding, cells were treated with CWP232228 or YB-0158 for 48 hours vs. DMSO control. Two hours before the end of the drug incubation period, a pulse of EdU was added to all cultures, according to manufacturer's protocol. Then, cells were formalin-fixed (2% v/v) and EdU-positive cells were fluorescently labeled following a click chemistry reaction. Nuclei were stained with Hoechst 33342. Image acquisition and EdU-positive cell scoring was done using an ImageXpress Pico High-Content imaging system (Molecular Devices), as described above.

Apoptosis detection assay

Apoptosis levels in DMSO and YB-0158-treated cells were determined using CellEvent Caspase-3/7 green detection reagent (Thermo Fisher) (Benoit et al., 2021). HT29 cells were plated at 5,000 cells per well in 96-well plates and maintained for 24 hours in standard growth media. Then, cells were treated with DMSO or YB-0158 for 48 hours. As a positive control, each cell line was treated with 1 μM of staurosporine for 6 h. Next, 5μM of the CellEvent™ Caspase 3/7 Green labeling reagent was added to each well and incubated for 30 min at 37 °C. Cells were washed twice with PBS and formalin-fixed (2% v/v) for 30 min. Hoechst 33342 was used to stain nuclei. Image acquisition and activated Caspase-3/7-positive cell scoring was done using an ImageXpress Pico High-Content imaging system (Molecular Devices), as described above.

Serial organoid formation assay

Assessment of tumor-initiating capacity in human colorectal tumor-derived specimens was performed using a serial organoid formation protocol involving CRC patient-derived specimens (Bergin et al., 2021). Patient-derived spheres enriched with colorectal CSCs were harvested and dissociated using TrypLE reagent (ThermoFisher) and passed through a 70-μm strainer to eliminate non-single-cell aggregates. Cell suspensions were mixed with Matrigel in sphere culture media (1:1 ratio) to get a 1-cell/μl density. Mixtures were immediately plated as 300 μl domes in 6-well plates and incubated for 15 minutes at 37°C for Matrigel polymerization. Then, 2.5mL of sphere media containing different doses of YB-0158 (0.125, 0.250, 0.500, 1.0 and 2.0μM) or vehicle control (DMSO) was added to each well. Drug treatment lasted for 7 days, followed

by a 7-day drug-free incubation period. At day-14, plates were imaged using an ImageXpress Pico high-content imaging system to determine organoid counts and size using CellReporterXpress software. For secondary passage experiments, control primary organoids and those remaining in treated wells were dissociated using a gentle dissociation reagent (STEMCELL Technologies) and re-plated as described above, but according to a 50-cell/μl density. Secondary organoids were grown for 14 days in sphere culture media with no further drug treatment. Then, secondary organoid counts were determined as described above.

Serial *in vivo* tumor transplantation assay

All *in vivo* procedures and protocols were approved by the University of Ottawa Animal Care Committee. Assessment of peptidomimetic small molecule capacity to target CSC functions *in vivo* was conducted in a serial syngeneic mouse tumor transplantation assay. Untreated MC38 cells (C57BL/6 background) were dissociated and re-suspended in a 1:1 HBSS:Matrigel mixture prior to subcutaneous injection into the flanks of the primary C57BL/6 recipient mice (6 to 8 weeks old females), at a density of $1x10^6$ cells per site. Seven days post-injection, daily doses of YB-0158 (100mg/kg), CWP232228 (100mg/kg), or control saline (HBSS vehicle) were intraperitoneally injected in tumor-bearing animals for 14 days. Primary tumour growth was measured on a daily basis following palpable tumor detection using a digital caliper. The ellipsoidal tumour volume was calculated according to V = (L x W x W)/2. Mice were scrutinized for potential changes in behavioral and clinical indicators, including weight loss, feces consistency, rectal bleeding, movement disorder, facial grimace, abnormal respiration, hunching, piloerection, agitation/aggressivity, food consumption and grooming habits during and after drug administration. At experimental day 21, primary tumours were surgically extracted, dissociated with 100U/ml of collagenase IV and 100μg/ml of DNase I, and passed through 70μm strainer to eliminate debris and cell clumps. Tumor cells were re-suspended in a 1:1 HBSS:Matrigel mixture and re-injected subcutaneously in the flanks of a secondary series of recipient mice. Secondary mice injected with tumor cells from control and drug-treated groups were maintained for 14 days without any treatments. At endpoint, secondary recipient mice were injected with 10nmoles of IRDye-800CW-2-deoxyglucose (IR800-2-DG) in the tail vein, and the presence/absence of secondary tumors was assessed by *in vivo* fluorescence imaging using an IVIS Spectrum In Vivo Imaging System (PerkinElmer). The final volume of secondary tumors was also measured using the caliper method, as above described.

QUANTIFICATION AND STATISTICAL ANALYSIS

Data is represented as the mean ± SEM. P-values ≤ 0.05 were considered significant. "n" denotes the number of times the data was replicated. All "n" numbers and scale bar length can be found in figure legends. Significant differences between groups were determined by statistical tests indicated in figure legends, using GraphPad Prism software. Fisher's exact test was used to determine statistical significance between two classifications.